

# Hypergraph Representations of scRNA-seq Data for Improved Clustering with Random Walks

Wan He\*,<sup>1</sup> Daniel I. Bolnick,<sup>2</sup> Samuel V. Scarpino,<sup>1,3,4</sup> and Tina Eliassi-Rad<sup>1,5,4,3</sup>

<sup>1</sup>*Network Science Institute, Northeastern University, Boston, MA, USA*

<sup>2</sup>*Department of Ecology and Evolutionary Biology, University of Connecticut Storrs CT, USA*

<sup>3</sup>*Vermont Complex Systems Institute, University of Vermont, Burlington, VT, USA*

<sup>4</sup>*Santa Fe Institute, Santa Fe, NM, USA*

<sup>5</sup>*Khoury College of Computer Sciences, Northeastern University, Boston, MA, USA*

Analysis of single-cell RNA sequencing data is often conducted through considering their network projections such as coexpression networks, primarily due to the abundant availability of network analysis tools for downstream tasks. However, this approach has several limitations. First, projecting scRNA-seq data into networks can result in the loss of higher-order information since it summarizes the gene expression profiles across cells into pairwise cell or gene similarities. Secondly, scRNA-seq data is often very sparse, but the constructed coexpression network projections are fully connected without sparsification, resulting in dense and inefficient data representation. Further, the sparsity of scRNA-seq data leads to co-occurrence of zero expression in a large proportion of the genes. Such zero-expression co-occurrence will be accounted as similarity in gene expression among cells by correlation methods such as Spearman's rank and Pearson's correlation coefficient and lead to an overestimation of coexpression.

To address these limitations, we propose conceptualizing scRNA-seq expression data as hypergraphs, which are generalized graphs in which the hyperedges can connect more than two vertices. This flexibility makes hypergraphs particularly well-suited for representing scRNA-seq data without requiring further transformation such as coexpression networks generation. In the context of scRNA-seq data, the hypergraph nodes represent cells and the edges represent genes. Specifically, each hyperedge connects to all the cells where the gene is actively expressed and records the expression of the gene across different cells. The hypergraph conceptualization enables us to explore the multi-way relationship beyond the pairwise interactions in coexpression networks for scRNA-seq data analysis while utilizing network analysis tools.

We propose two novel hypergraph random walk-based cell clustering methods: (1) the Dual-Importance Preference Hypergraph Walk (DIPHW) and (2) the Coexpression and Memory-Integrated Dual-Importance Preference Hypergraph Walk (CoMem-DIPHW). They outperform widely used and established methods in terms of clustering accuracy on both simulated and real scRNA-seq datasets. The improvement brought by our proposed methods is especially significant when the data modularity is weak. By conceptualizing the scRNA-seq data as hypergraphs, our methods provide a more nuanced representation of gene expression data, allowing the incorporation of network perspectives without the information loss caused by enforcing a unipartite coexpression network projection. Furthermore, one of the clustering methods we propose, CoMem-DIPHW, incorporates the gene coexpression network, cell coexpression network, and the cell-gene expression hypergraph from the single-cell abundance counts data altogether for embedding computation. This approach accounts for both the local level information from single-cell level gene expression and the global level information from the pairwise similarity in the two coexpression networks.

## I. INTRODUCTION

Network analysis has become a popular tool for studying complex systems in biology, as a reflection of the combinatorial interaction mechanism of biomolecules. Its applications include functional analysis [1–4] and interaction prediction in protein-protein interaction (PPI) networks [5–7], regulator identification and pathway analysis in gene regulatory networks [8–10], disease modeling, prediction, and intervention in epidemiology [11–13], and cell type identification in co-expression networks [14–17].

While these methods employed unipartite networks to aid analysis, it is often overlooked that unipartite networks are often not the most natural or information-preserving representation of the complex system we are interested in studying since many complex systems involve interactions from more than one type of entities. Examples include protein-protein interaction (PPI) networks where the nodes are proteins and edges could be physical contacts among proteins or functional interactions in biological pathways, gene regulatory networks (GRNs) where nodes represent genes and a directed edge exists if one gene regulates the expression of another gene, coexpression networks where the nodes are genes, cells, or tissues and the weighted edges indicate similarity in expression profile between node pairs.

An example of a network that captures higher-order interactions between different entity types is the bipartite network, where nodes are partitioned by two separate groups, and edges only connect nodes from different groups. Bipartite networks are particularly suitable for modeling systems where two types of entities interact, such as authors and papers in a collaboration network [18], recommendation systems [19] where nodes represent users and the recommending items, and specifically in

biology, plant-pollinators and predator-prey interaction networks [20] in community ecology studies, microbe-host interaction networks [21] in microbiology, drug-protein interaction networks [22], and transcription factor-gene networks in genomics.

However, instead of modelling these systems using network models that could capture higher order interactions, most often, a unipartite network projection is chosen such that the system could be analyzed with the abundant network analysis methods developed based on unipartite networks [14, 23]. For example, in the bipartite representation of a drug interaction network, the two classes of nodes represent drugs and protein targets respectively. A drug node and a protein node are connected if the drug targets the protein. In its unipartite transformed network, a drug-drug interaction network could be constructed based on shared targets. Similarly, in the bipartite protein complex network, proteins and biological functions are two types of nodes that are connected if the proteins are involved in the biological function. Yet, in the unipartite representation of the protein complex network, the clique graph of the original bipartite graph is constructed where the only class of nodes are the proteins and the protein nodes are connected if they are in the same complex that performs a biological function. Unipartite representations fail to capture the biological functions associated with groups of proteins. While unipartite projections can reveal relationships between nodes of the same type in a bipartite network, they often obscure the specificity of these interactions.

Single-cell RNA sequencing (scRNA-seq) has enabled the profiling of gene expression at the individual cell level [24–27], whereas conventional bulk tissue RNA sequencing measures expression at the tissue level, averaging gene expression over an ensemble of cells. Cell type identification, as one of the most important downstream tasks in single-cell RNA-seq (scRNA-seq) data analysis [28], has applications across biology and medicine, including tracing the trajectories of distinct cell lineages in development for cell differentiation studies [29], tissue heterogeneity analysis for cancer research [30–32], immune cell profiling for therapy development [33–36], and biomarker discovery for diagnosis.

However, cell type identification often relies on conventional transcriptomic data analysis pipelines such as WGCNA [14], Scanpy [17] and Seurat [15, 16]. These packages embed the cell-gene expression to a unipartite graph structure such as the coexpression network or the K-nearest neighbor (KNN) graph, which draw edges between the cell pairs based on their similarity, followed by unipartite graph partitioning algorithms to detect closely related cell clusters for cell type identification in the scRNA-seq data. The similarity or distance between cell pairs in these unipartite networks are mostly measured by the correlation between their expression profiles across all genes. Similarly, gene coexpression networks are constructed by summarizing information regarding similarity in the expression profiles of genes across different cells. However, these unipartite projections of the original scRNA-seq expression data have two limitations: Firstly, while gene and cell coexpression networks capture pairwise expression similarity among cells, or among genes, higher-dimensional information such as the expression level of a specific gene in a specific cell is lost. Secondly, scRNA-seq data are often sparse, sometimes with less than 10% of the entries being non-zero [37, 38], compared to 60-90% for bulk-tissue data. Constructing the co-expression unipartite projection networks results in a fully-connected (edge density=100%) network, which is an inefficient representation of the originally sparse expression data. Further, during the correlation computation, the zero entries in the data points, i.e., genes not detected in a cell due to technical issues (dropouts) or the genes that in fact do not express in that cell (biological zeros), play as important a role as the positive entries, namely, genes that do express in a cell, since they are weighted the same in Pearson’s correlation computation. The high sparsity of such data makes the projection prone to problems, causing inflated correlations and hence misleading signals in the co-expression networks, as will be elaborated further in III C. Besides, identifying whether the zero inflation in scRNA-seq data is due to technical dropouts or true biological absence is a challenging task [37, 39, 40].

Given the issues with unipartite projections, it is crucial to explore alternative network representations that can accurately reflect the scRNA-seq data. Hypergraphs offer a neat solution by representing multi-way relationships in scRNA-seq directly, without the need for further data projection. Moreover, each bipartite graph can also be represented as a hypergraph, by modelling one set of entities as nodes and the other as hyperedges, offering a generalized representation of high-order interactions. In this work, we propose a hypergraph-based approach to analyze scRNA-seq data to overcome the limitations of unipartite projections.

## II. METHODS

In scRNA-seq analysis, clustering cells based on co-expression networks projected from count data is a common approach for cell type identification. However, as discussed in III C, the correlation inflation problem associated with co-expression networks caused by the induced sparsity in scRNA-seq data, as well as information loss from projecting a hypergraph to a unipartite simple graph, motivated us to look beyond co-expression networks for scRNA-seq analysis.

We conceptualize scRNA-seq data as a hypergraph  $\mathcal{H}$ . In this framework, we propose a hypergraph random walk-based clustering method that models the relationships between cells and genes in the cell-gene expression abundance count data. Specifically, each cell is represented as a node, and each gene is represented as a hyperedge. Each hyperedge captures the expression profile of a gene across all cells, allowing us to apply hypergraph based analysis tools without enduring the loss of information caused by projecting the scRNA-seq data into a simple unipartite graph, e.g. the co-expression networks. We design random walk algorithms that capture cell-cell interactions by sampling the cell-to-gene and gene-to-cell paths in the conceptualized hypergraph. The random walk sampling probability distribution is designed to account for the specific cell-gene expressions via the edge-dependent vertex selection probability and the vertex-dependent edge selection probability. The sam-

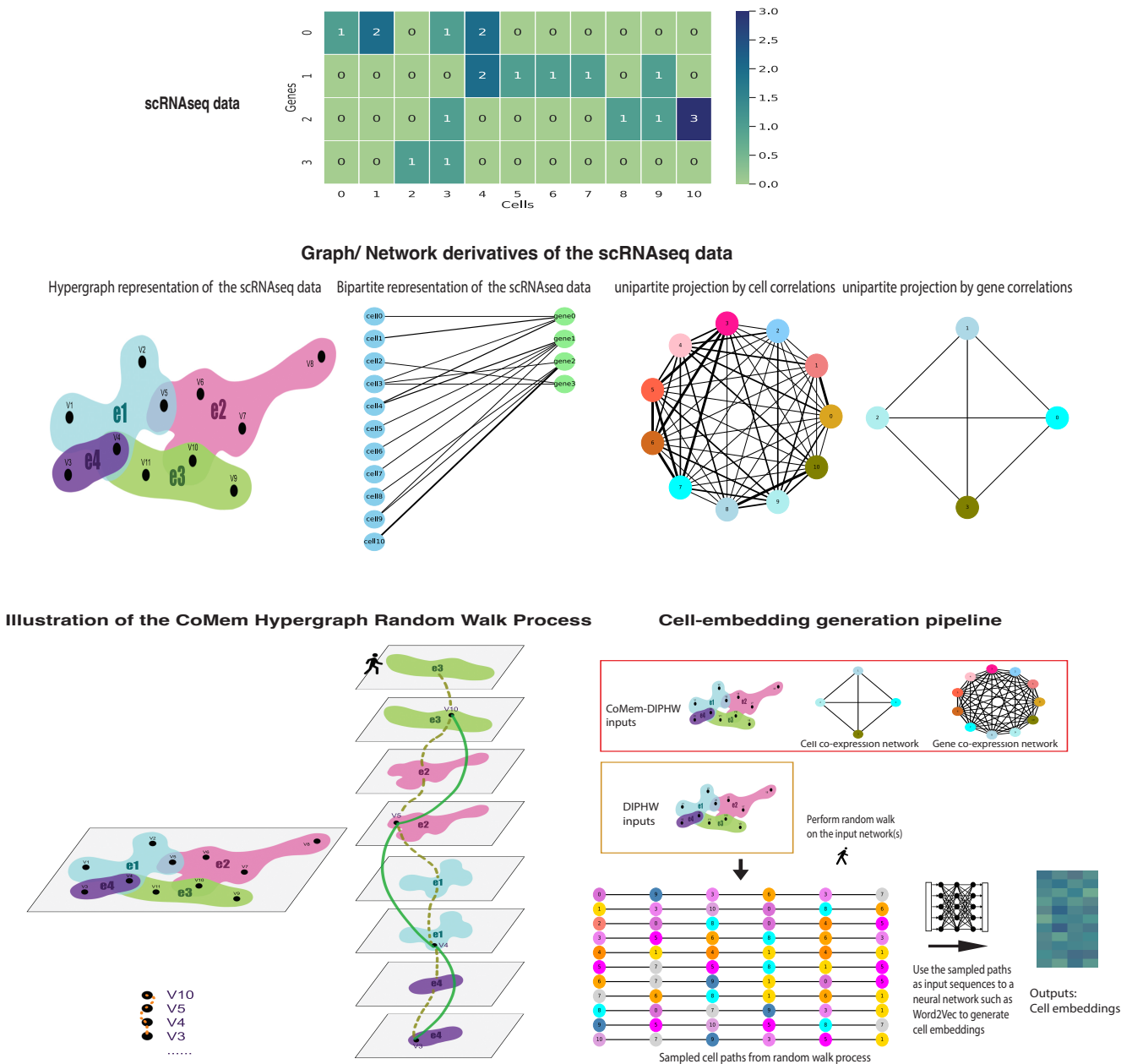


FIG. 1. Hypergraph Random Walk Illustration. The scRNA-seq cell-gene expression data is conceptualized as a hypergraph, where nodes represent cells and edges represent genes. The expression level of a gene in a cell is captured by the weight of a node in an edge. Random walks are performed on the hypergraph by alternatingly considering the probability of the walker choosing a node given an edge, and choosing an edge given the current node the walker is at. In the second proposed method, the Coexpression and Memory-Integrated Dual-Importance Preference Hypergraph Walk (CoMem-DIPHW), a memory mechanism is leveraged by considering the probability of choosing the next visiting node given the current edge and the previously visited node, and similarly, choosing the next visiting edge given the current node and the previously visited edge. The cell coexpression network and the gene coexpression network serve as the node similarity and edge similarity matrix to aid memory incorporation during the walk. A small neural network (word2vec) is applied to the sampled node paths from the hypergraph random walk to compute the cell embeddings. Finally, cell clustering is achieved by clustering the obtained cell embeddings by their similarities.

pled paths embed information regarding the amplified expression level of a gene in a cell, both in comparison to the expression levels of other genes in that cell and to the expression levels of the same gene in other cells. As a step further, CoMem-DIPHW (the Coexpression and Memory-Integrated Dual-Importance Preference Hypergraph Walk), the second hypergraph-based random walk algorithm proposed for clustering, incorporates a memory mechanism that takes into account both the conceptualized hypergraph from the scRNA-seq expression data, and the two projected unipartite coexpression networks, i.e. the cell and gene coexpression network, for cell-cell interaction sampling. The sampled cell-cell interaction paths would then be fed to a small language model (Word2Vec) to generate efficient numerical representations (embeddings) of the cells. These embeddings would then be used to cluster the cells by applying a clustering algorithm such as UMAP or tSNE to group the cells based on their similarity in the embedded space.

We emphasize that this hypergraph conceptualization of the scRNA-seq data does not require further transformation on the data and consequently would not result in any information loss or computation cost from converting the scRNA-seq into coexpression networks. We remark that a matrix is a 2-dimensional array structured for organizing information related to two variables. Thus a matrix could naturally be conceptualized as a hypergraph by considering the column variables as nodes and the row variables as edges and vice versa.

### A. Hypergraph representation

The single-cell RNA sequencing (scRNA-seq) data can be conceptualized as a hypergraph  $\mathcal{H} = (V, E)$ , where:

- $V$  represents the vertex set corresponding to the cells profiled in the experiment.
- $E$  denotes the hyperedge set representing genes, with each hyperedge  $e \in E$  connecting to all cells  $\in V$  in which the gene  $e$  is actively expressed.

The incidence matrix  $\mathbf{I}_{\mathcal{H}}$  of the hypergraph  $\mathcal{H}$  is constructed such that  $\mathbf{I}_{\mathcal{H}}(v, e)$  is given by the expression level, i.e. abundance counts, of gene  $e$  in cell  $v$ .

### B. Bipartite representation

We chose the hypergraph conceptualization over bipartite representation for consistency since the DIPHW algorithm we introduced is an extension of the edge-dependent vertex weight hypergraph random walk (EDVW) [41]. DIPHW extended EDVW hypergraph random walk [41] with a vertex-dependent edge selection probability, as well as a preference exponent for clustering acceleration.

A bipartite conceptualization could be adopted for our proposed methods DIPHW, CoMem, and CoMem-DIPHW by considering the incidence matrix  $\mathbf{I}_{\mathcal{H}}$  of the hypergraph  $\mathcal{H}$  as a bipartite graph. The two sets of nodes in the bipartite representation are the set of cells  $V$  and the set of genes  $E$ . Similarly, each gene is connected to all cells in which it is actively expressed, with weights corresponding to the expression level. This alternative representation allows for the use of bipartite graph algorithms and conceptualization for analyses. For example, we used Barber’s bipartite modularity [42] to assess the how the clustering performance of different algorithms vary with modularity of the underlying scRNA-seq dataset.

### C. Method 1: Dual-Importance Preference (DIP) Hypergraph Walk (DIPHW)

We introduced a novel hypergraph random walk approach, the *Dual-Importance Preference (DIP) Hypergraph Walk (DIPHW)*, highlighting the consideration of both the relative importance of edges to nodes and nodes to edges, or importance of genes relative to cells and cell to genes, along with a preference exponent for faster clustering. In a hypergraph random walk process, the walker typically alternates between transitioning from a hyperedge to a node and from a node to a hyperedge, following the node-to-edge transition probabilities  $P_{E|V}(e, v)$  and edge-to-node transition probabilities  $P_{V|E}(v, e)$ . In the hypergraph random walk with edge-dependent vertex weight (EDVW) by Chitra and Raphael (2019) [41], the edge-to-node transition probability is edge-dependent, but the node-to-edge transition probability does not consider the previously visited node, i.e.,  $P_{V|E}(v, e) = P_E(e)$  for all  $v \in V$ . As a natural extension to EDVW, we defined the node-to-edge transition probability to be vertex-dependent in DIPHW, and used a preference exponent to accelerate the clustering process. The modified random walk process is described as follows: at time  $t$ , assuming the random walker is at vertex  $v_t$ , the walker proceeds by iteratively selecting the next hyperedge and the subsequent vertex within that hyperedge to transition to, based on the following probabilities:



Notation	Description
$\mathcal{H}$	Hypergraph
$\mathbf{I}_{\mathcal{H}}$	Incidence matrix of the hypergraph $\mathcal{H}$
$V$	Set of all nodes (cells)
$E$	Set of all hyperedges (genes) in the hypergraph
$G_V$	Cell co-expression network
$G_E$	Gene co-expression network
$\Gamma_e(v)$	Weight of node $v$ in hyperedge $e$ , i.e., expression of $gene_e$ in $cell_v$ .
$P(V E)$	Probability of selecting vertex $v$ in edge $e$
$P(E V)$	Probability of selecting edge $e$ given vertex $v$
$P(E_{t+1} E_t, V)$	Probability of transitioning from node $v$ in edge $\alpha$ to edge $\beta$
$P(V_{t+1} E, V_t)$	Probability of selecting node $w$ from edge $\beta$ after transitioning from node $v$
$P(v_t \rightarrow w_{t+1})$	Unipartite node-to-node transition probability of the multilayer network random walk process

TABLE I. Hypergraph Random Walk Notation Table

### 1. Node-to-Hyperedge Transition Probability:

The probability of selecting hyperedge  $e_{t+1}$  given that the walker is currently at vertex  $v_t$  is defined as:

$$P_{E|V}(v_t \rightarrow e_{t+1}) = \frac{\omega(e_{t+1})\gamma_{e_{t+1}}(v_t)}{\sum_{e' \in E(v_t)} \omega(e')\gamma_{e'}(v_t)}$$

In the context of scRNA-seq cell clustering, this cell-dependent gene selection probability depends on the relative expression level of a gene in a cell compared to the expression of other genes in the same cell.

### 2. Hyperedge-to-Node Transition Probability:

Upon the walker's arrival at hyperedge  $e_{t+1}$ , the probability of moving to vertex  $v_{t+1} \in e_{t+1}$  is defined as:

$$P_{V|E}(e_{t+1} \rightarrow v_{t+1}) = \frac{\gamma_{e_{t+1}}^\alpha(v_{t+1})}{\sum_{v' \in e_{t+1}} \gamma_{e_{t+1}}^\alpha(v')}$$

In the context of scRNA-seq cell clustering, the transition from a gene to a cell is based on the relative expression level of a gene in a cell, amplified by the preference exponent for faster clustering convergence, and normalized by the same gene's expression in other cells.

3. *Node-to-Node Transition Probability:* Marginalizing over all possible hyperedges the walker can traverse gives the unipartite node-to-node transition probability of DIPHW. This probability is used for sampling the random walk node paths which capture the structural and relational information of the original hypergraph and are subsequently used as inputs to a neural network for cell embedding computation.

$$P(v_t \rightarrow v_{t+1}) = \sum_{e \in E} P_{E|V}(e|v_t)P_{V|E}(v_{t+1}|e).$$

Substituting the expressions for  $P_{E|V}(e_{t+1}|v_t)$  and  $P_{V|E}(v_{t+1}|e_{t+1})$ , we get:

$$P(v_t \rightarrow v_{t+1}) = \sum_{e_{t+1} \in E} \frac{\omega(e_{t+1})\gamma_{e_{t+1}}(v_t)}{\sum_{e' \in E} \omega(e')\gamma_{e'}(v_t)} \frac{\gamma_{e_{t+1}}^\alpha(v_{t+1})}{\sum_{v' \in e_{t+1}} \gamma_{e_{t+1}}^\alpha(v')}$$

The expression of node-to-node transition probability could be simplified by removing reference to any particular time points as,

$$P(u \rightarrow v) = \sum_{e \in E(u)} \frac{\omega(e)\gamma_e(u)}{\sum_{e' \in E} \omega(e')\gamma_{e'}(u)} \frac{\gamma_e(v)}{\sum_{u' \in e} \gamma_e(u')}$$

#### 4. Node-to-Node Transition Probability in Vectorized Format:

For efficient computation, the  $|V| \times |V|$  node-to-node transition probability matrix  $P_{V|V}$  could be written in the vectorized form as,

$$P = D_{E|V}^{-1} W_{E|V} D_{V|E}^{-1} W_{V|E}$$

The vectorization circumvents the need for explicit iteration and reduces the computation time. Here,  $W_{E|V} = \mathbf{I}_{\mathcal{H}}^T W_E$  is the  $|V| \times |E|$  node-to-edge transition weight matrix where column  $e$  of  $W_{E|V}$  is the vertex weights in hyperedge  $e$  multiplied by the weight of hyperedge  $e$ . Similarly,  $W_{V|E}$  represents the edge-to-node transition weight matrix before normalization, with dimensions  $|E| \times |V|$ . Each entry in this matrix is obtained by raising the corresponding edge-dependent vertex weight to the power determined by the preference exponent  $\alpha$ , expressed as  $W_{V|E} = (\mathbf{I}_{\mathcal{H}}^\alpha)$ , where  $w_{ve} = [\mathbf{I}_{\mathcal{H}}(e, v)]^\alpha$ . Finally,  $D_{E|V}$  and  $D_{V|E}$  are diagonal normalizing matrices used to normalize the distribution of the transition from vertex-to-edge and edge-to-vertex respective so that the probability distribution sums to 1.

#### D. Method 2: Coexpression and Memory-Integrated Dual-Importance Preference Hypergraph Walk (CoMem-DIPHW)

In this section, we introduce the Coexpression and Memory-Integrated Dual-Importance Preference Hypergraph Walk (CoMem-DIPHW) designed to integrate scRNA-seq expression data and its coexpression networks for improved cell embedding computation. CoMem-DIPHW builds upon the Dual-Importance Preference Hypergraph Walk (DIPHW) and incorporates a memory mechanism to consider previously visited nodes and edges during transitions.

*a. Hypergraph Representation and the unipartite network projections of the scRNA-seq data* We remark that a matrix can be directly interpreted as the incidence matrix of a hypergraph to represent the relationship between two variables, without the need for any additional computation. Moreover, we can construct two correlation networks as derivatives of the matrix. In each correlation network, the nodes correspond to one of the two variables, and the edges represent the correlations between the node pairs of the corresponding variable. These two unipartite correlation network projections embed global level information that summarizes the association between node pairs through their correlation.

*b. The Node and Edge Similarity Networks: Cell and Gene Coexpression Networks and their construction* Using scRNA-seq data, we construct two coexpression networks: the gene-coexpression network (GCN)  $G_E$  and the cell-coexpression network (CCN)  $G_V$ . In the GCN, genes are represented as nodes, and edges correspond to correlation coefficients between gene pairs, indicating the similarity between their expression profiles. Similarly, in the CCN, cells are represented as nodes, and edges correspond to correlation coefficients between cell pairs. These two co-expression networks are unipartite projection networks of the original scRNA-seq expression data, with edge weights providing a summary statistic of pairwise similarity in expression profiles. Spearman’s rank coefficient was chosen to measure pairwise similarity of expression profiles as it is a non-parametric measure that captures non-linearity compared to Pearson’s correlation coefficient. The cell and gene coexpression networks respectively are the node and edge similarity networks derived from the hypergraph. These two unipartite correlation network projections embed global level information that summarizes the association between cell and gene pairs through their correlation.

*c. Memory-Integrated Random Walk* Our proposed random walk process CoMem-DIPHW integrates a memory component by considering the similarity between consecutively visited nodes and edges. This memory mechanism adjusts the transition probabilities such that the node-to-edge transition probability depends on the previous edge visited, and the edge-to-node transition probability depends on the previous node visited. The node-node and edge-edge dependencies are incorporated through the node-node and edge-edge similarity networks, which are the two correlation networks derived from the original matrix. The memory incorporation allows both the local and global structures in the hypergraph to be captured by the walk. Moreover, the memory mechanism constrains the hypergraph walker to focus on network(cell-gene) interactions among similar nodes(cells) and edges(genes) to better uncover modularity within the data.

*d. Capturing Global and Local Geometry* In our proposed CoMem-DIP-HW random walk, we leverage global information from unipartite projections—the gene-coexpression network  $G_E$  and the cell-coexpression network  $G_V$ —along with local information from the hypergraph structure in the cell-gene scRNA-seq expression data to enhance clustering performance. The coexpression networks serve as node and edge similarity matrices, facilitating the memory-incorporated hypergraph random walk. For cell clustering and cell type identification in scRNA-seq data, cells are modeled as nodes and genes as hyperedges. The hypergraph represents the expression profiles of cells across genes, where each hyperedge (gene) connects to nodes (cells) in which it is expressed. The weight of connection in a hyperedge to each node (cell) is determined by the gene’s expression

level in that cell. The cell coexpression network  $G_V$  functions as the node similarity matrix, with  $G_{V_{i,j}}$  representing the similarity between the expression profiles of cell pair  $i$  and  $j$ . Similarly, the gene coexpression network  $G_E$  serves as the edge similarity matrix, representing the similarity in expression profile between pairs of genes across different cells. Each entry in these matrices aggregates information from the expression profiles of pairs of cells or genes into pairwise similarities, providing a global perspective through unipartite network projections. However, specific expression levels of genes in individual cells, representing local information, are lost in these projected networks. Therefore, our proposed hypergraph random walk methods aim to integrate global information while preserving local information, to achieve more accurate cell type identification.

*e. Formulation* The random walk process in CoMem-DIPHW is formulated as follows:

Let  $G_V$  be the vertex similarity matrix, where  $G_V(v, w)$  quantifies the similarity between vertices  $v$  and  $w$ . Similarly, let  $G_E$  be the edge similarity matrix, where each element  $G_E(e, f)$  represents the similarity between edge  $e$  and  $f$ .

#### Method 2.0: CoMem

1. The probability of selecting vertex  $v$  in edge  $e$  is:

$$P_{V|E}(e \rightarrow v) = \frac{\Gamma_e(v)}{\sum_{u \in e} \Gamma_e(u)}$$

2. The probability of selecting edge  $e$  given vertex  $v$  is:

$$P_{E|V}(v \rightarrow e) = \frac{\Gamma_e(v)}{\sum_{e \in E} \Gamma_e(v)}$$

3. The probability of transitioning from node  $v$  in edge  $e_1$  to edge  $e_2$ , considering edge similarity, is given by:

$$P_{E_{t+1}|V, E_t}(e_2|v, e_1) = \frac{G_E(e_1, e_2)P(e_2|v)}{\sum_{e' \in E} G_E(e_1, e')P(e'|v)}$$

4. Similarly, the probability of selecting node  $w$  from edge  $e$  after transitioning from node  $v$ , incorporating node similarity and the node-edge connection, is formulated as:

$$P_{V_{t+1}|E, V_t}(w|e, v) = \frac{G_V(v, w)P(w|e)}{\sum_{w' \in e} G_V(v, w')P(w'|e)}$$

Finally, the unipartite node-to-node transition probability of the multilayer network random walk process is:

$$P_{V_t \rightarrow V_{t+1}}(v, w) \propto \sum_{e_1, e_2 \in E} P_{V|E}(v|e_1)P_{E_2|V, E_1}(e_2|v, e_1)P_{V_{t+1}|E, V_t}(w|e_2, v)$$

To encourage exploration and ensure non-lazy walks, we modify the node and edge similarity graphs such that the diagonal elements are set to zero. This ensures that during the random walk, the random walker does not remain at the same edge or node in consecutive steps.

#### Method 2.1: CoMem based on DIPHW

Further, for CoMem-DIPHW, we incorporate DIPHW proposed in section II C to CoMem walk II D 0 e. We define

- The probability of selecting vertex  $v$  in edge  $e$  is:

$$P_{V|E}(e \rightarrow v) = \frac{\gamma_e(v)^\alpha}{\sum_{v' \in e} \gamma_e(v')^\alpha}$$

- The probability of selecting edge  $e$  given vertex  $v$  is:

$$P_{E|V}(v \rightarrow e) = \frac{\omega(e)\gamma_e(v)}{\sum_{e' \in E(v)} \omega(e')\gamma_{e'}(v)}$$

The other probability distributions are the same as defined in section II D 0 e

### E. Complexity Analysis

*a. DIPHW* The computation cost of each element  $P(u \rightarrow v)$  in the  $|V| \times |V|$  node-to-node transition probability matrix is  $O(|E|)$  when the intermediate matrices for the node-to-edge and edge-to-node transition probabilities  $P_{E|V}(e|u)$  and  $P_{V|E}(v|e)$  are precomputed. Constructing the entire  $|V| \times |V|$  node-to-node transition probability matrix thus involves computing these probabilities for all node pairs, resulting in an overall time complexity of  $O(|V|^2 \cdot |E|)$ .

For efficient computation, the  $|V| \times |V|$  node-to-node transition probability matrix  $P_{V|V}$  in vectorized form is given by:

$$P_{V|V} = D_{E|V}^{-1} W_{E|V} D_{V|E}^{-1} W_{V|E}$$

While the theoretical complexity remains  $O(|E|^2 \cdot |V| + |E| \cdot |V|^2)$  for the vectorized approach, it utilizes parallel computation and is significantly faster and hence more suitable for large datasets. The memory complexity is  $O(|E| \cdot |V|)$  for the node-to-edge and edge-to-node transition probability matrices.

*b. CoMem-DIPHW* The time complexity of CoMem-DIPHW is  $O(|E|^2 \cdot |V|^2)$ , as for each node pair, the memory-incorporated transition traverses all possible edges that could have arrived at the first node and all possible edges that could then connect the first node with the second node. The memory complexity is  $O(|E|^2 \cdot |V| + |E| \cdot |V|^2)$  for the memory incorporated node-to-edge and edge-to-node transition probability matrices.

## III. EXPERIMENTS AND RESULTS

### A. Baseline Methods

To evaluate the performance of DIPHW and CoMem-DIPHW, we compared them to several widely used and established cell clustering methods, including five other embedding-based methods, including PCA [43], Node2Vec [44], EDVW [41], UMAP, and tSNE, and four unipartite-graph-based community detection methods: Louvain, Greedy Modularity, Infomap, and Leiden. These methods are adopted by popular scRNA-seq analysis packages such as Seurat [15], WGCNA [14] and Scanpy [17]. We provide a summary of these methods in table II. For a fair comparison under consistent conditions, we focus on the core clustering algorithms, rather than specific implementations in packages such as Seurat and Scanpy. This allows us to evaluate the clustering capabilities of each method independently of any additional preprocessing or optimization steps in the package implementations.

### B. Data and Preprocessing

The data used in this study consists of both simulated data and publicly available scRNA-seq datasets. The simulated data was generated using our proposed simulation algorithm, which is described in detail in the Methods section. The code used to generate the simulated data and perform the analysis is available on GitHub at [<https://github.com/wanhe13/CoMem-DIPHW>]. We have also provided a detailed README file to guide users through the process of running the code and reproducing our results. For preprocessing, the raw single-cell RNA-seq data was preprocessed to remove genes and cells with zero expression. After filtering, the data was normalized such that the total counts per cell were equal to account for differences in sequencing depth among cells. For empirical analysis, we used four publicly available scRNA-seq datasets: human brain [45], human pancreas [46], mouse brain [47], and mouse pancreas [48] and a curated benchmarking dataset that comes with ground truth cell labels [49]. A major challenge in scRNA-seq analysis is the lack of reliable ground truth for cell type annotation, which complicates the evaluation of clustering algorithms. Traditional cell type annotations in scRNA-seq data are conducted manually by identifying established marker genes, which depends on results from differentially expressed genes in each cluster found by an unsupervised clustering algorithm [50–52]. Hence, the cell type annotation depends on clustering results inherently, creating a circular logic that introduces bias towards the clustering method used to obtain the cell type annotations [53, 54]. To achieve more reliable evaluation of the methods comparison, we utilized the mixture control benchmarking dataset [49] where ground truth is incorporated through cell line identity.

### C. Sparsity-Induced Correlation Inflation in scRNA-seq Co-expression Networks

The zero inflation problem in single-cell RNA sequencing (scRNA-seq) data analysis refers to the excessive number of zero counts (or "dropouts") observed in the data. These zeros could either be a result of technical limitation in detecting low abundance transcripts (false negatives), or true absence biological zeros (true negatives) [37, 39, 40]. In a scRNA-seq data, when the

Method	Data Input	Key Concepts	Packages
<b>Embedding-Based Methods</b>			
DIPHW	Hypergraph incidence matrix	Sample node sequences by dual-importance preference hypergraph random walk, followed by computing embeddings using these node sequences via word2vec	Our proposed method
CoMem	Hypergraph incidence matrix and its two unipartite network projections	Sample node sequences by a hypergraph random walk process that considers node and edge similarity via a memory mechanism, followed by computing embeddings using these node sequences via word2vec	Our proposed method
CoMem-DIPHW	Hypergraph incidence matrix and its two unipartite network projections	Integration of CoMem and DIPHW for enhanced performance	Our proposed method
EDVW	Hypergraph incidence matrix	Sample node sequences by edge-dependent vertex weight hypergraph random walk followed by computing embeddings using these node sequences via word2vec	Proposed by [41] and not implemented in scRNA-seq packages
PCA	Matrix	Projects data onto orthogonal components that maximize variance	Seurat, Scanpy, SC3, Cell Ranger
Node2Vec	Unipartite graph	Sample node sequences by random walk followed by computing embeddings using these node sequences via word2vec	Proposed by [44] and not implemented in scRNA-seq packages
UMAP	Matrix	dimension reduction and preserves more global structure than t-SNE	Seurat, Scanpy
t-SNE	Matrix	Compute pairwise similarity distribution of the data points with a Gaussian kernel and then learn a lower dimensional distribution that reflects the similarity by minimizing the KL-divergence between the similarity distribution in the Gaussian kernel and the learned low-dimension distance distribution. Maximize KL-divergence between the embedded	Seurat, Scanpy
<b>Community Detection Methods</b>			
Louvain	Unipartite network	Modularity optimization by local optimization (assigning nodes to neighbouring communities that lead to maximum modularity increase) and community aggregation (creates a new network where the nodes are the communities)	Seurat, Scanpy, WGCNA
Greedy Modularity	Unipartite network	Modularity optimization by bottom-up community merging	igraph
Infomap	Unipartite network	Information flow maximization	igraph
Leiden	Unipartite network	Modularity optimization and enforcing connected nodes in a community	igraph

TABLE II. Comparison of clustering methods evaluated in experiments

individually profiled cell expression are merged to create a unified dataset, all genes are included in the expression profile of every cell. However, since typically cells express different sets of genes, the inclusion of all genes in the merged dataset introduces significant sparsity to the scRNA-seq data. Consequentially, when the scRNA-seq data is analyzed through the constructed coexpression networks, these induced zeros can lead to inflated correlation coefficients between cells or genes. This occurs because during the coexpression network construction, the edge weights represent correlation between the expression profiles and are often computed by Pearson’s correlation coefficient or Spearman’s rank correlation coefficient. In these commonly adopted correlation measures, the zeros are treated as a magnitude of expression in the same way as the non-zeros. As a result, if two expression profiles share a large number of common zeros, their correlation will be inflated since the common zeros will be considered as a token of their expression homogeneity, which can lead to an overestimation of the similarity between expression profiles. This problem is particularly prominent at the single-cell level compared to bulk tissue RNAseq data, as the percentage of genes that are expressed at the single-cell level in the aggregated scRNA-seq data is much smaller than at the tissue level, leading to a higher degree of induced data sparsity.

In the experiment shown in Fig. 2, we investigate the impact of induced sparsity in scRNA-seq data on correlation coefficients, which impacts the interpretation of gene and cell connection in co-expression networks. We demonstrate that the induced zeros leads to an inflation of the correlation coefficients between cells or genes. To simulate this effect, we generated gene expression data with a fixed base size and appended varying proportions of zeros to mimic the different degrees of sparsity that can be induced in scRNA-seq data when merging cell expression profiles. We repeated this process 100 times and calculated the 95% confidence interval of the correlations for each sparsity level. We show that as the proportion of zeros appended to the data increases, the correlation coefficient also increases, leading to an overestimation of the similarity between expression

profiles. Our results show that as the level of induced sparsity increases, the correlation coefficient also increases, leading to an overestimation of the similarity between expression profiles. These findings highlight the importance of considering zero inflation in scRNA-seq data analysis and the need for accurate representation of the underlying data structures.

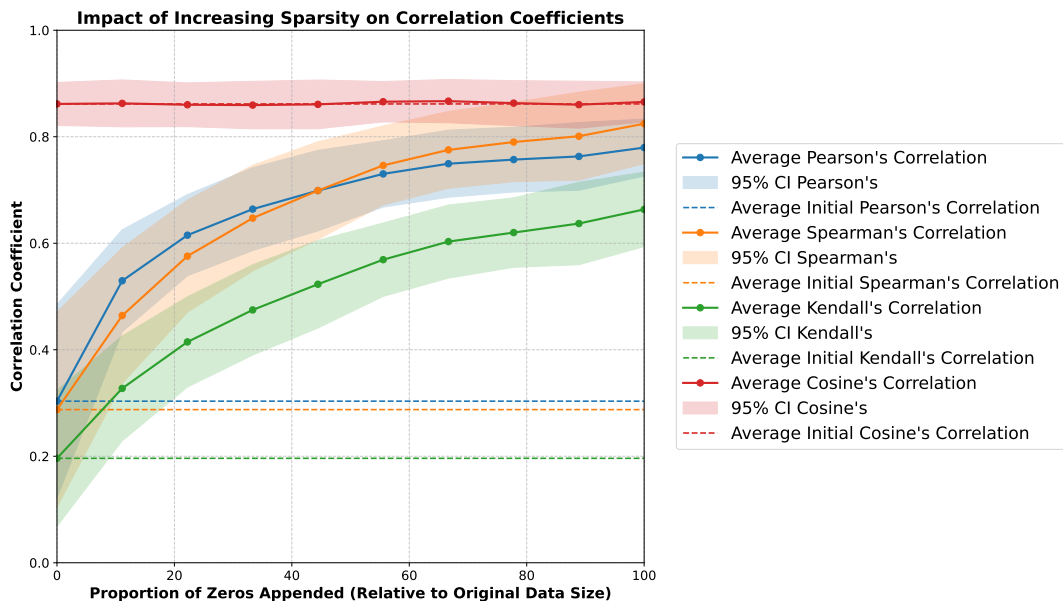


FIG. 2. Impact of Increased Sparsity on Correlation Coefficients. This figure illustrates the relationship between the proportion of zeros appended to the expression profile (representing increased sparsity) and the resulting correlation coefficients. Shaded areas indicate the 95% confidence intervals around the average correlation values. The dashed lines mark the average initial correlation without added sparsity, serving as a benchmark for comparison.

#### D. Simulation Analysis Results

In our study, we developed an algorithm to simulate data that mimics the characteristics of scRNA-seq expression data. Besides the underlying assumption of within-cell-type homogeneous expression that governs most of if not all of the cell clustering methods, we also incorporated between-cell-type cross talk [55–59] by integrating configurable intermodular covariance, density and signal strength to the simulation model. The algorithm generates a sparse matrix representing the simulated scRNA-seq expression data, with numerous user-configurable parameters, including number of modules, module density, shape, background signal strength, modular signal strength, intermodular signal strength, inter-modular covariance and noise level. This method is implemented as a function in our codebase and is available for use by other researchers.

Our simulation model is designed with high flexibility to accommodate different types of scRNA-seq data. For instance, the model can simulate both deeply sequenced datasets with high density (up to 50%) and shallowly sequenced datasets with low density (as low as 1%) [60]. The proportion of non-housekeeping genes can be adjusted by changing the number of differentially expressed genes in each module. Moreover, the variance in module sizes and the number of coexpressed genes in each cell type can be configured by setting different variances for the Poisson distribution used in the embedded module simulation. The modules embedded in the simulated data can be configured with higher density and average signal strength to model the expression profiles of biomarker genes that are highly expressed in certain cell types. This allows us to mimic the sparsity and modularity of real scRNA-seq data, where a small number of genes are highly expressed in specific cell types. Alternatively, the embedding modules can also be user-specified without using the embedded module simulation.

##### 1. Evaluation Metrics

To evaluate the performance of the clustering methods on datasets with known ground truth, we employed two widely used metrics for measuring coherence between the identified clusters and the ground truth clusters: Adjusted Rand Index (ARI) and Normalized Mutual Information (NMI). Both metrics are invariant to permutations, with a score of 0 representing random labeling and a score of 1 indicating identical clusters. For embedding-based methods that do not directly assign cluster membership,

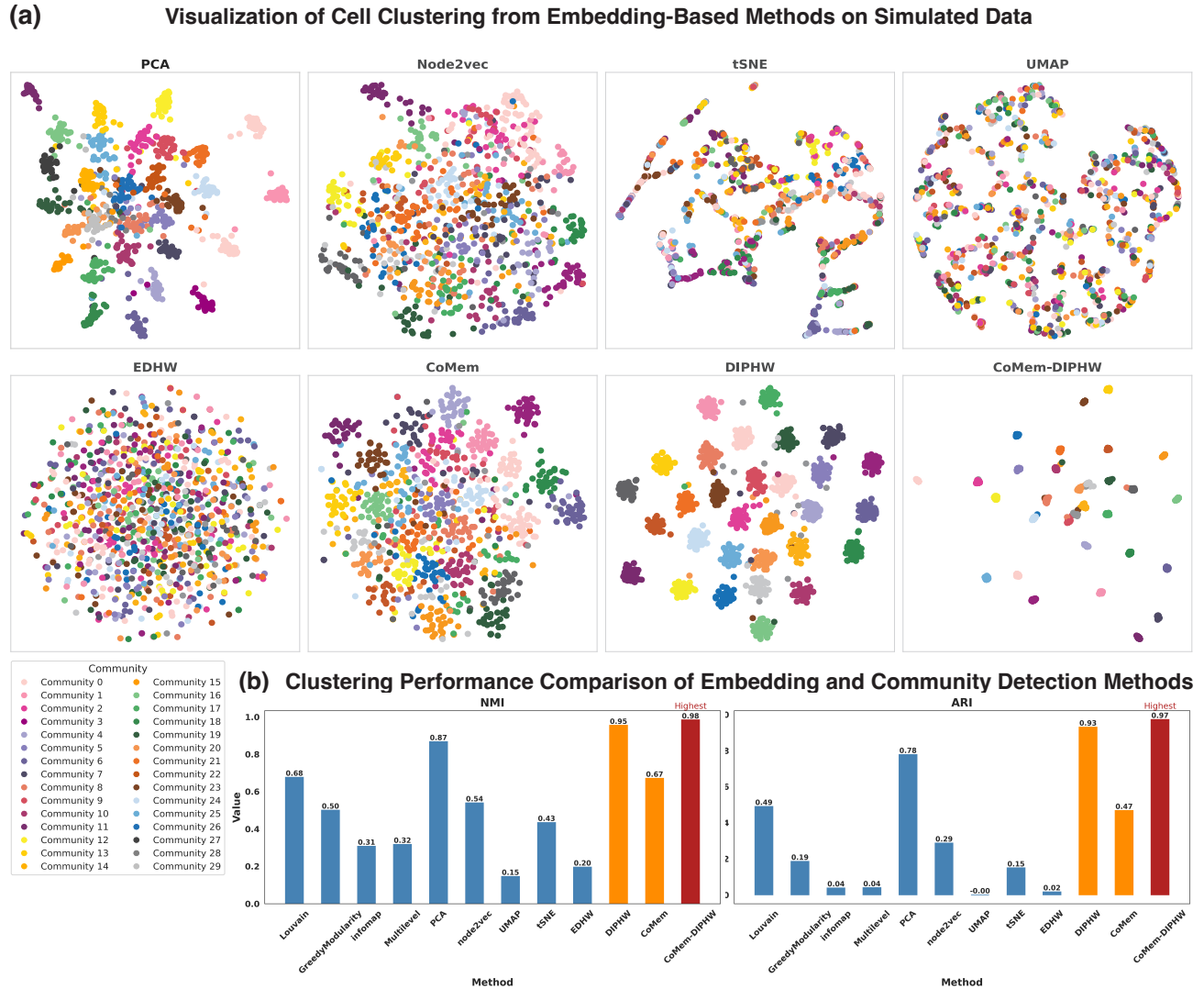


FIG. 3. Clustering Results on Simulated scRNA-seq Data Using Embedding-based and Community Detection Methods. (a) UMAP visualization of the embedding clustering results, with colors indicating ground truth cell cluster membership. (b) NMI and ARI bar plots comparing the performance of the embedding and community detection methods. DIPHW and CoMem-DIPHW demonstrated the highest degree of internal cohesion within clusters and the best cluster separation, as evidenced by both the embedding visualizations and the ARI and NMI scores.

we used K-means to partition the embedded data into clusters.

## 2. Embedding Visualizations

We present the visualizations and clustering performance of the embeddings in Fig.3 by DIPHW, CoMem, and CoMem-DIPHW, compared against five other embedding-based methods, including PCA, Node2Vec, EDVW [41], UMAP, and tSNE, and four community detection methods: Louvain, Greedy Modularity, Infomap, and Leiden, applied to simulated single-cell RNA sequencing (scRNA-seq) data. Embedding-based methods compute representations of the cells in a lower-dimensional space while preserving their global geometry [61–63], followed by UMAP for cluster visualisation, whereas community detection methods identify clusters (communities) based on the structures of the unipartite networks projected from the scRNA-seq data. Although tSNE and UMAP are typically not used as a standalone embedding algorithms, we have included them in the comparison for reference, as they are adopted by popular packages in single-cell analysis, such as Seurat [15, 16], Scanpy [17], SC3 [64] and Cell Ranger [26], and there has been ongoing discussions about using them as the main clustering methods in

scRNA-seq analysis [65, 66]. We note that the strength of tSNE and UMAP is in preserving local structures, such as the nearest neighbors [65, 67], while UMAP can also preserve global distance [67]. However, they are not designed to group data into clusters with high internal cohesion. Therefore, they are generally used in conjunction with other clustering methods as visualizing tools that map computed embeddings to a 2D space for evaluation.

The results are compared with the ground truth cell type membership in the embedding visualization and in the NMI and ARI bar plots. UMAP was applied to the embeddings produced by the dimensionality-reduction clustering algorithms for visualization. Each dot represents a cell, with its color indicating the ground truth cell cluster membership and its position representing the embedding. As illustrated, DIPHW and CoMem-DIPHW demonstrated the highest degree of internal cohesion within clusters and the best cluster separation, as evidenced by both the embedding visualizations and the ARI and NMI scores. We also evaluate the performance of CoMem, which shares the same memory mechanism of CoMem-DIPHW but without the dual importance (edge-dependent vertex selection probability and vertex-dependent edge selection probability) or preference exponent, as a baseline to show the improvement brought by integrating the hypergraph-based random walk DIPHW with the memory mechanism in CoMem.

The parameters used to simulate the scRNA-seq data used in this experiment were chosen to capture the main characteristics and underlying assumptions of scRNA-seq analysis. Although they may not perfectly represent the values observed in real scRNA-seq data, the parameters are set to provide a challenging enough clustering task to differentiate the performance of the clustering algorithms being evaluated. The inter-module density is set at 0.1, and inter-module connection probability at 0.6 to represent cell-type cross-talk [56–59, 68] with a relatively weaker expression signal density than within cell-type expression. The baseline gene expression level is 10, with an average module expression of 20 to create a contrast to within cell-type expression signal strength.

### 3. Clustering Performance vs. Bipartite Modularity

We further evaluated the performance of these clustering methods under varying data modularity conditions. The modularity variation was controlled by two key parameters: the average number of coexpressed genes per cell type and the number of embedded cell modules. Additionally, we implemented Barber’s bipartite modularity [42], as shown by the barplots in Fig.4 (a), to help quantify modularity of the underlying data for clustering and analyze the association between modularity and clustering performance. As shown in Fig.4 (a), clustering performance generally improves with increased data modularity. The modularity bar plots in Fig.4 (a) and heatmap visualization in Fig.4 (b) demonstrate that the simulated scRNA-seq data displays stronger modularity when the average number of coexpressed genes per cell type is greater or when the number of modules is smaller. Our proposed methods—DIPHW, CoMem, and CoMem-DIPHW—consistently outperformed all other clustering methods that use unipartite network projections, including Node2vec, and community detection-based methods such as Louvain and Greedy Modularity. Notably, CoMem-DIPHW consistently demonstrated superior performance across almost all parameter settings, with its advantage being particularly pronounced under weak data modularity conditions.

### 4. Clustering Performance Comparison under strong and weak data modularity parameter regimes

In Fig.5 and 6, we present the performance of our proposed clustering methods, highlighted in red and yellow, compared against the baseline methods under strong and weak data modularity parameter regimes. Clustering performance is measured using ARI and NMI. Each experiment was repeated 100 times per parameter setting, with error bars indicating the 95% confidence interval of the results. The barplots display the mean value (top) and average ranking (bottom) of each method by performance, ordered by their average NMI or ARI scores.

Data modularity is evaluated based on the average number of co-expressed genes per module and the number of modules in the simulated scRNA-seq data. Weak modularity is modelled by a small number of co-expressed genes per module or a large number of modules embedded in the data. Conversely, strong modularity is represented by a large number of co-expressed genes per module or a small number of embedded modules. To model weak modularity, we embedded 70, 80, 90, and 100 modules in the simulated data, while for strong modularity, we embedded 10, 20, 30, and 40 modules. For the number of co-expressed genes per module, we used 70, 80, 90, and 100 genes to represent strong modularity, and 10, 20, 30, and 40 genes to represent weak modularity.

Out of the 16 tested scenarios, CoMem-DIPHW or DIPHW consistently ranked first by ARI and in 10 scenarios by NMI. Our hypergraph-based methods showed significant advantages in weak modularity regimes, where data structures are harder to detect. Under comparatively strong modularity conditions, several methods (PCA, CoMem-DIPHW, CoMem, node2vec, DIPHW, and Louvain) performed well, with average NMI scores above 0.9. Notably, PCA slightly outperformed CoMem-DIPHW by NMI under strong modularity, with differences in NMI scores ranging from 0.01 to 0.02.



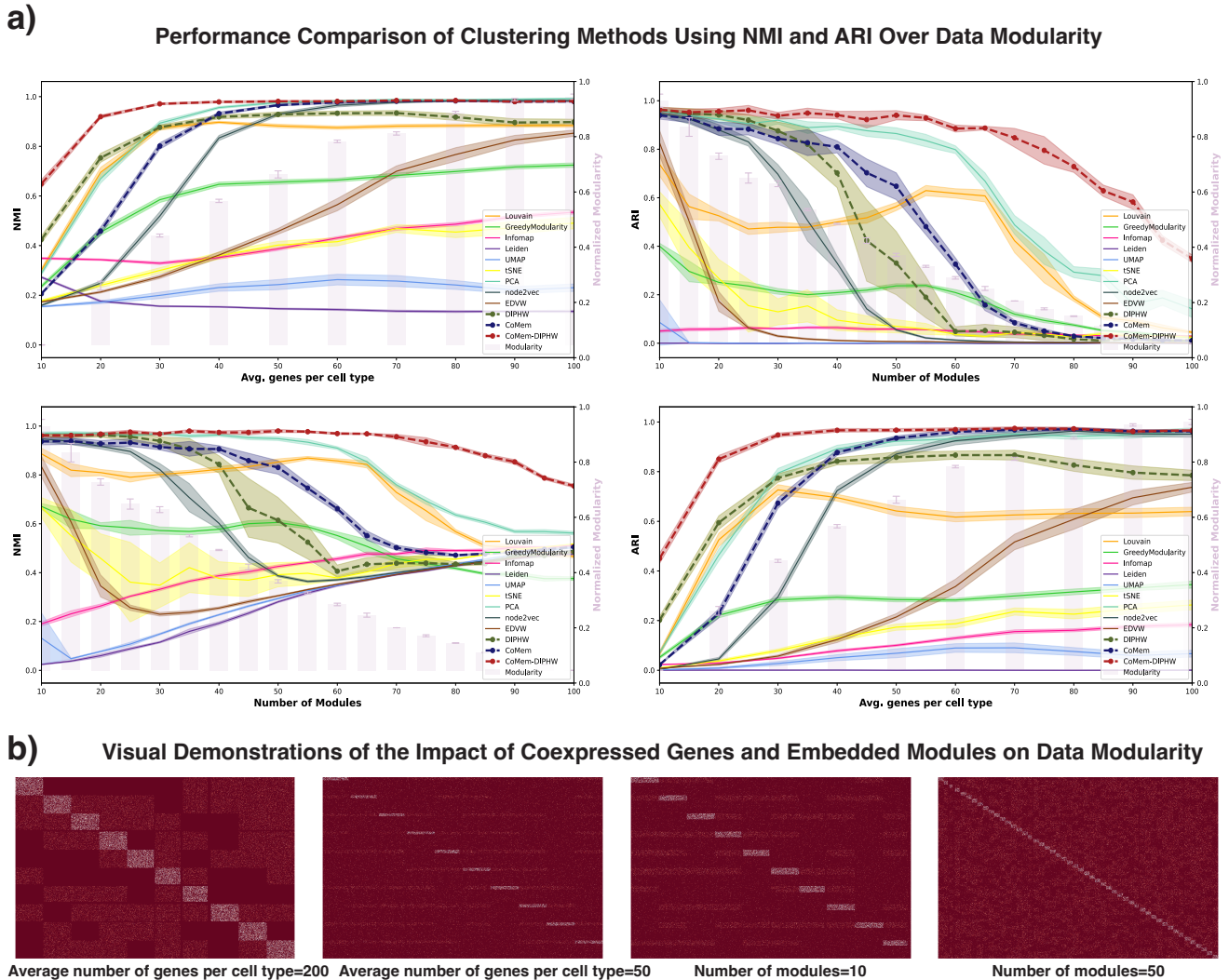


FIG. 4. Performance Comparison of Clustering Methods on Simulated scRNA-seq Data Modularity. (a) Performance of clustering methods measured by ARI and NMI, across different levels of data modularity. The x-axis represents parameters determining data modularity, including the average number of coexpressed genes per cell type and the number of embedded modules. Our proposed methods DIPHW, CoMem, and CoMem-DIPHW are highlighted by the dashed lines. CoMem-DIPHW, in particular, maintains great performance and is least affected by the decrease in modularity, performing significantly better even under conditions of extremely weak modularity. Experiments were repeated 10 times for each parameter setting, and the 95% confidence intervals (CIs) are shown. The bar plots represent Barber's bipartite modularity, normalized such that the most modular graphs have modularity = 1. (b) Visualization of how the average number of coexpressed genes per cell type and the number of embedded modules affect the modularity of simulated scRNA-seq data. Stronger modularity is exhibited with a higher average number of coexpressed genes per cell type and fewer modules.

### 5. Evaluating the Impact of Correlation Methods on Network-Based Clustering Performance

There are two primary strategies for handling the shared zeros in the cell expression profiles in scRNA-seq data during correlation computation. The first strategy, exemplified by cosine similarity, is to ignore the shared zeros. This means that the inactive expression (zeros) does not contribute to the similarity between cells. However, our experiments indicate that this strategy results in significantly worse clustering performance. Understandably, the absence of expression in the same genes between cell pairs provides valuable information about cellular similarity and should not be disregarded entirely.

In Table. III D 5, we evaluated how coexpression networks generated by different correlation computation methods lead to varying performance by various network-based clustering methods. The correlation methods considered were Pearson's,

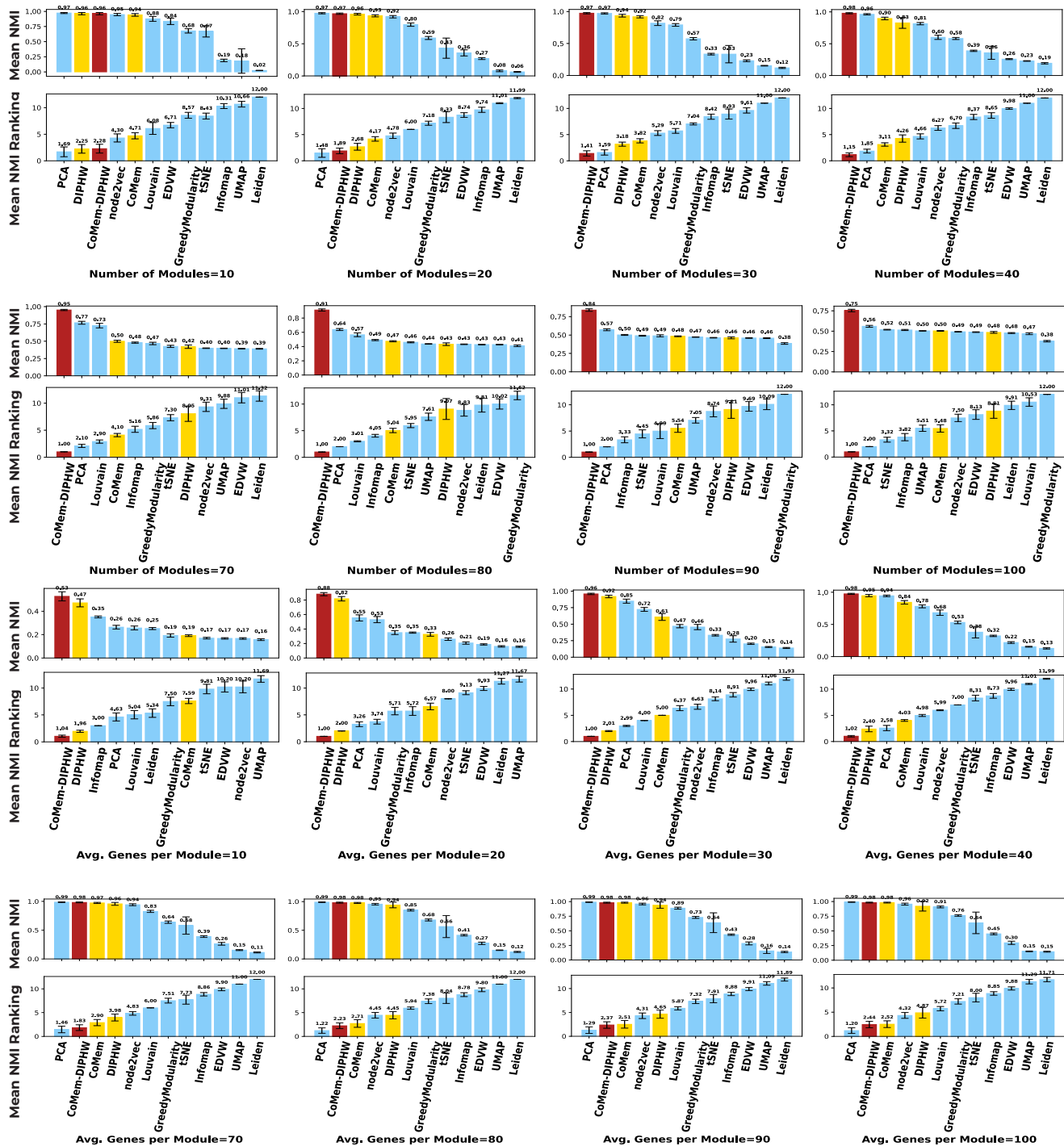


FIG. 5. Clustering Performance Comparison by NMI Under Strong and Weak Data Modularity Parameter Regimes. The barplots show the mean NMI (top) and average ranking (bottom) of each method, ordered by their average NMI. Our proposed methods, highlighted in red and yellow, ranked first by NMI in 10 out of the 16 scenarios. Each experiment was repeated 100 times per parameter setting, with error bars representing the 95% confidence interval. Hypergraph-based methods, including CoMem-DIPHW and DIPHW, showed significant advantages in weak modularity regimes, where data structures are harder to detect. Under strong modularity conditions, most of the methods (e.g., PCA, CoMem-DIPHW, CoMem, node2vec, DIPHW, and Louvain) performed well, achieving average NMI scores above 0.9. Notably, PCA slightly outperformed CoMem-DIPHW by NMI under strong modularity, by 0.01 to 0.02.

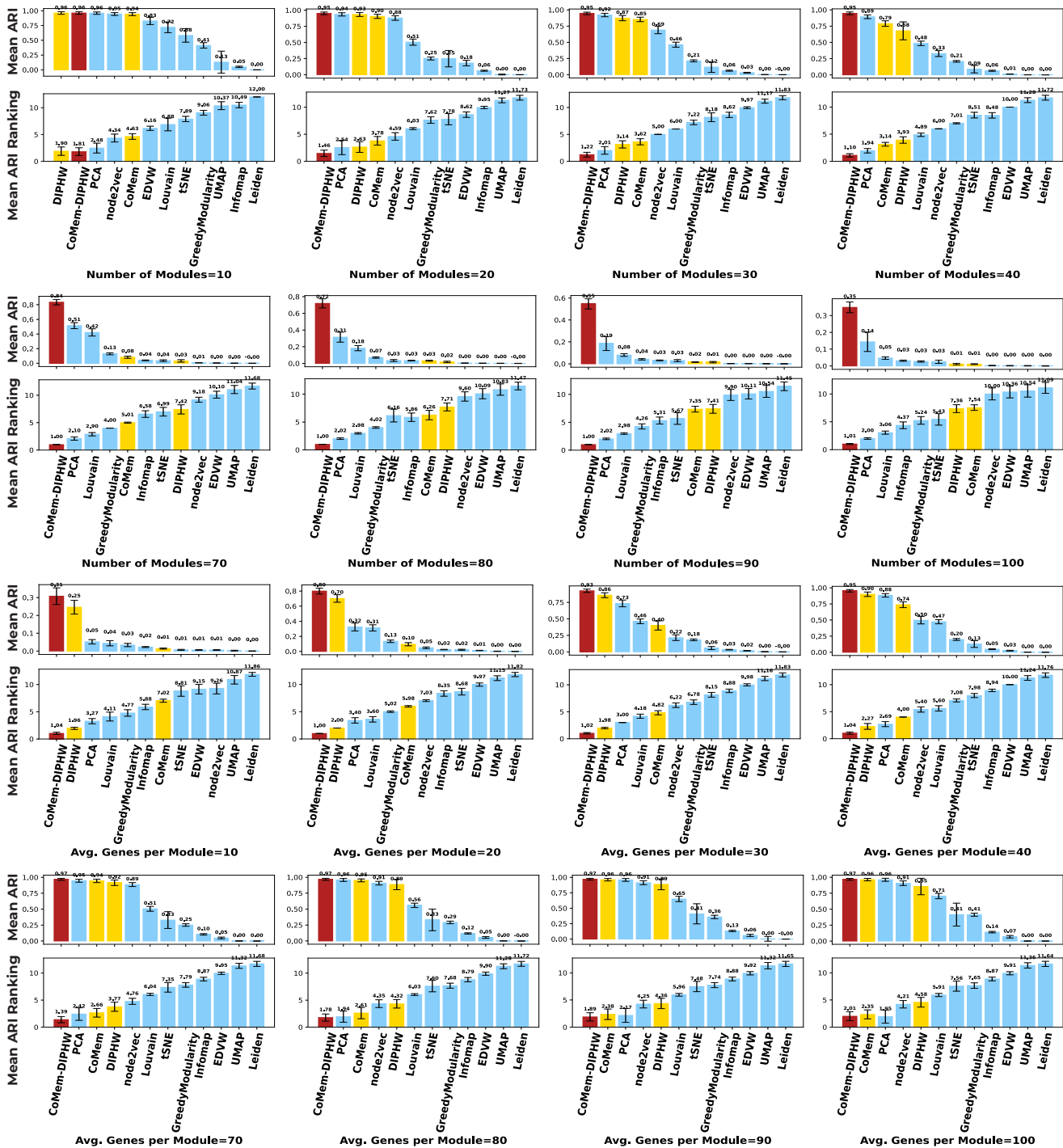


FIG. 6. Clustering Performance Comparison by ARI Under Strong and Weak Data Modularity Parameter Regimes. Our proposed methods, highlighted in red and yellow, consistently ranked first by ARI in 16 scenarios. Each experiment was repeated 100 times per parameter setting, with error bars representing the 95% confidence interval.

Spearman's, Kendall's Tau, and cosine similarity. Our results show that cosine similarity often led to the worst clustering results among the correlation computation methods tested.

The primary implication of this experiment is that both strategies have inherent drawbacks when dealing with the sparsity of scRNA-seq data. Ignoring zeros misses out on significant information, while treating them as homogeneity signals inflates correlations and introduces noise. Ignoring the shared zeros in cell expression profiles, as cosine similarity does, is not an effective strategy and results in the worst performance. Conversely, the methods that consider all the shared zeros in the expression

	Pearson	Cosine	Spearman	Kendall
Louvain (ARI)	0.495	0.450	0.438	<b>0.427</b>
eigenvector (ARI)	0.002	<b>0.000</b>	0.003	0.005
Multilevel (ARI)	<b>0.032</b>	0.034	0.034	0.035
Louvain (NMI)	0.690	0.660	0.659	<b>0.655</b>
eigenvector (NMI)	0.097	<b>0.060</b>	0.082	0.091
Multilevel (NMI)	0.305	<b>0.289</b>	0.325	0.319

TABLE III. Impact of Correlation Methods on Network-Based Clustering Performance. The table evaluates the impact of correlation computation methods—Pearson’s, Spearman’s, Kendall’s Tau, and cosine similarity—on the performance of various network-based clustering methods. The correlation computation method resulting in the worst clustering performance is marked in bold. Cosine similarity, which ignores shared zeros in cell expression profiles, often resulted in the worst clustering performance. These results show that, although using correlation computation methods that treat zeros the same as non-zero signals could inflate correlations, ignoring these zeros, as in cosine similarity, can lead to worse performance.

profiles as an indication of cell homogeneity —such as Pearson’s, Spearman’s, and Kendall’s Tau— are neglecting the fact that many shared zeros are merely a result of the high dimensionality of scRNA-seq data. When sequencing results from multiple cells are merged, many zero entries are introduced since different cells often express different sets of genes. Consequently, cell correlations are inflated by these methods when data is sparse. The clustering outcomes from these methods are suboptimal when compared with approaches that do not require correlation computation, such as CoMem, DIPHW, and PCA, potentially due to misleading signals in the inflated correlation networks [3, 4, 5, 6]. Our results suggest that alternative approaches, such as hypergraph-based methods, provide a better solution by circumventing the need for unipartite network projections and avoiding the intricacy associated with handling zeros in correlation computations.

Finally, to demonstrate the generalizability of the proposed methods, we evaluated their performance on 648 simulated scRNA-seq datasets with different sizes, modules, inter-module densities, and signal strengths. The dataset variations included sizes ranging from 1000 to 3000 genes, 30 to 1000 cells, module counts from 20 to 60, inter-module density levels from 0.1% to 0.5%, and signal strengths from 15 to 20. As shown in Fig., CoMem-DIPHW outperformed the other algorithms both in terms of average ARI and NMI values and rankings.

### E. Empirical Analysis Results

We evaluated the performance of our proposed method, CoMem-DIPHW, using two benchmarking datasets from scMixology [49]. These datasets provide ground truth labels for cell type annotation based on human lung adenocarcinoma cell lines. As shown in Table IV, CoMem-DIPHW outperformed other methods, particularly on the 5-class dataset, achieving the highest NMI and ARI scores. In comparison, Louvain showed strong performance on the 3-class dataset but underperformed significantly on the 5-class dataset. Among the methods evaluated, PCA, CoMem, and CoMem-DIPHW consistently demonstrated robust performance across both datasets.

Dataset	Leiden	Greedy Modularity	Louvain HT	Infomap	Multilevel	PCA	EDVW	Node2Vec	DIPHW	CoMem	CoMem_DIPHW
scMixology 5 class NMI	0.7917	0.7852	0.4499	0.4355	0.4484	0.9700	0.7556	0.9020	0.8386	0.9666	<b>0.9729</b>
scMixology 5 class ARI	0.6746	0.6645	0.3373	0.3002	0.3319	0.9835	0.6689	0.9366	0.7308	0.9799	<b>0.9847</b>
scMixology NMI	<b>0.9864</b>	0.7193	0.3806	0.3843	0.3813	0.9810	0.6433	0.9743	0.9381	0.9742	0.9797
scMixology ARI	<b>0.9933</b>	0.5836	0.1721	0.2327	0.1730	0.9898	0.6443	0.9868	0.9617	0.9866	0.9900

TABLE IV. A comparison of NMI and ARI across clustering methods for the scMixology [49] benchmark datasets. CoMem and CoMem-DIPHW shows robust performance across both datasets.

For datasets without ground truth annotations—human pancreas, mouse pancreas, human brain, and mouse brain—we conducted differential expression (DE) analysis based on clustering results. We discuss our findings from the human pancreas dataset in detail, followed by a brief overview of results from the other datasets. To evaluate the clustering performance of various methods applied to human pancreas scRNA-seq data, we assessed the across-cluster differentiation in the average expression of the most differentially expressed (DE) genes for each cluster, as shown in Fig. 7. The goal was to determine whether the most DE genes identified for each cluster by each clustering method are indeed differentially expressed in their respective clusters compared to others. This experiment serves as an evaluation of clustering performance, helping us assess whether the methods can effectively capture differentiable groupings. Each row represents a specific clustering method, and each column corresponds to the expression of the top DE genes of a cluster identified by that method. Each subplot shows how the top 10 differentially expressed genes from one cluster behave across all clusters, using average expression levels. The x-axis indicates the cluster

id and the y-axis represents the average expression levels of the DE genes. Only clustering methods that produced fewer than 50 clusters are included in the figure. For example, Infomap, which produced 878 poorly defined clusters, was excluded. On the other hand, Leiden community detection identified fewer clusters with exclusively distinctive expression patterns, though they lacked the resolution necessary for finer-grained cell type identification analysis. Among the embedding-based clustering methods, CoMem and CoMem-DIPHW consistently showed distinctive expression in the corresponding cluster.

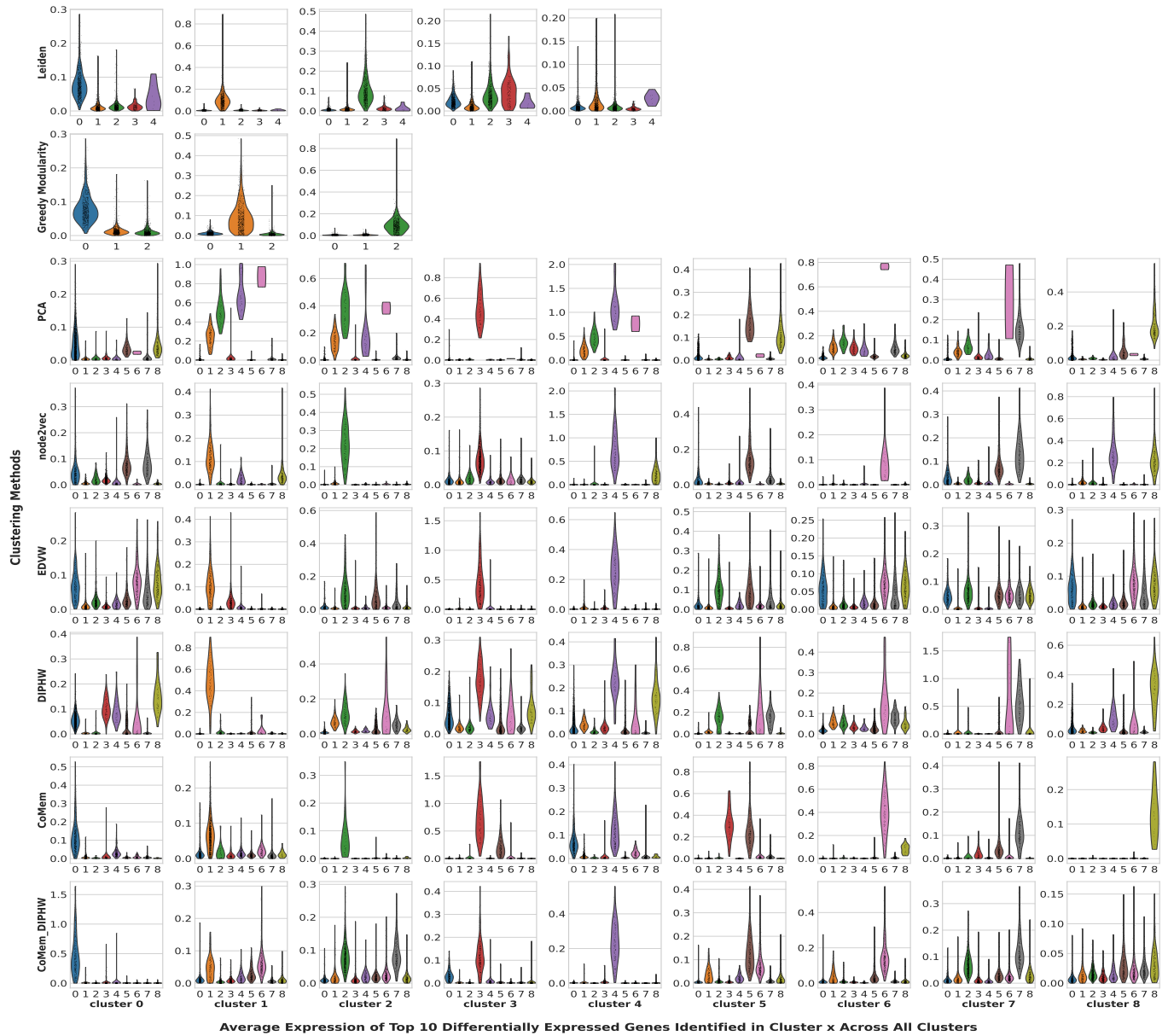


FIG. 7. Differential gene expression profiles across clustering methods in human pancreas scRNAseq data. The clustering performance is assessed by the differential expression (DE) of the top 10 DE genes identified for each cluster. Each row represents a clustering method, and each column corresponds to the top 10 differentially expressed (DE) genes of a specific cluster. Violin plots show the distribution of average expression levels of the top 10 DE genes across all clusters. Only clustering methods producing fewer than 50 clusters are included. Community detection methods, Leiden and greedy modularity, which yielded 4 and 3 clusters respectively, is included with fewer columns due to the lower number of clusters identified. CoMem and CoMem-DIPHW consistently showed distinctive expressions in the corresponding cluster.

We used canonical gene markers to tentatively label the cell clusters found by CoMem-DIPHW. The markers used include: GCG (alpha cells), INS (beta cells), SST (delta cells), PPY (PP cells), PRSS1 (acinar cells), KRT19 (ductal cells), COL1A1 (mesenchymal cells), and ESAM (endothelial cells) as reported in the original study of the human pancreas scRNA-seq data [46]. As shown in Fig. 8, each cell-type specific marker was distinctly expressed in a cohesive and well-defined cluster in the



embedding generated by CoMem and CoMem-DIPHW. These findings demonstrate the ability of CoMem and CoMem-DIPHW to produce biologically meaningful clusters. Notably, node2vec performed comparably well in generating cell embeddings distinguishable by cell type, suggesting the importance of incorporating coexpression networks when computing cell embeddings. In contrast, PCA, EDVW, and DIPHW did not perform well on this task. The embeddings of different clusters found by PCA lacked clear boundaries. EDVE and DIPHW failed to separate these cell types in the embedded space.

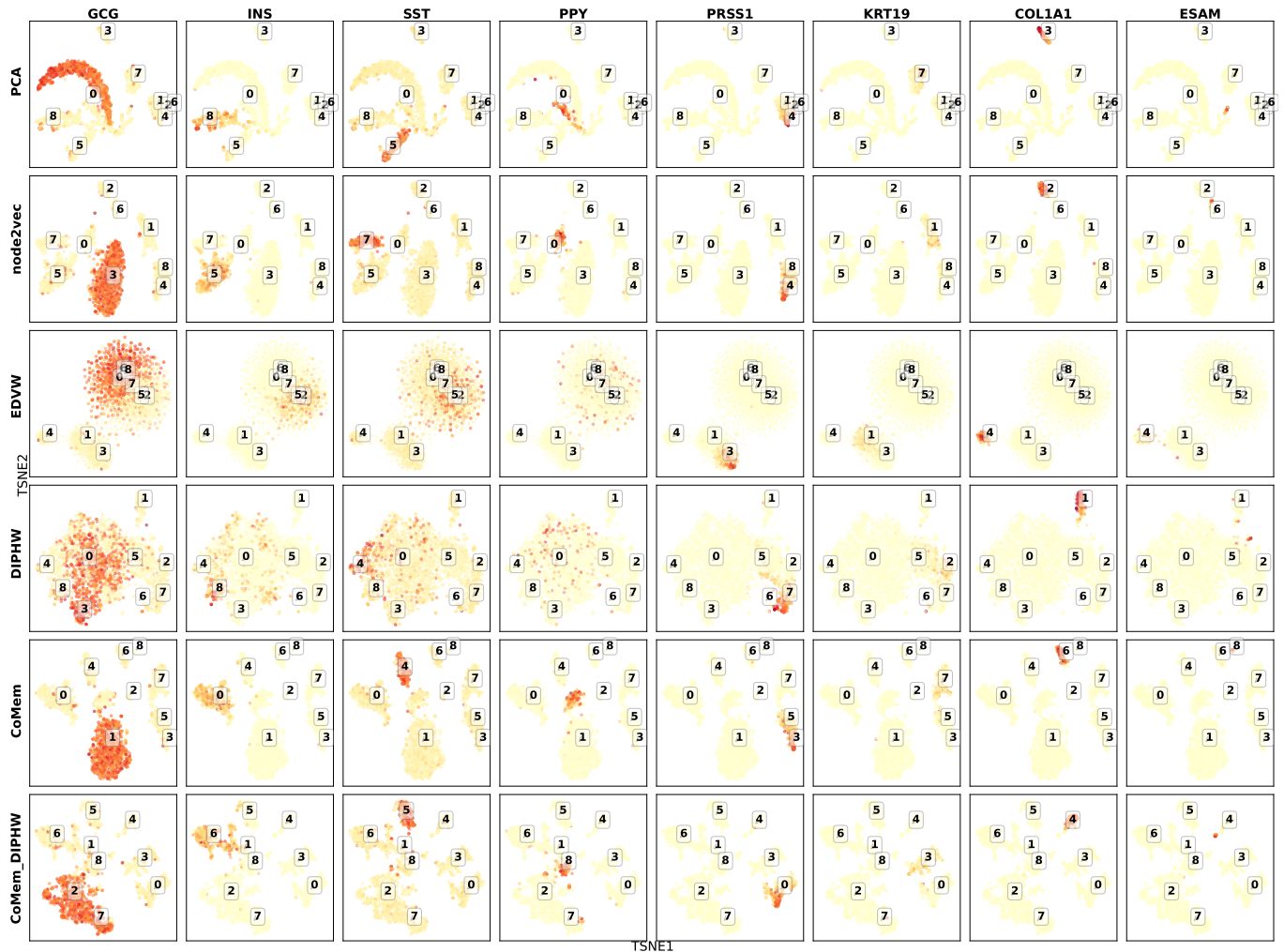


FIG. 8. Expression of Human Pancreas Cell-type Specific Marker Genes in Clusters Identified by Various Clustering Methods. The t-SNE visualizations show cell embeddings found by various clustering methods. Each column corresponds to the canonical marker of a cell type. The color intensity of the cell embeddings shows gene expression level, with redder colors indicating higher expression. Each subplot shows the expression level of a cell-type specific human pancreas marker gene in the embedding computed by a clustering method. The cell-type specific markers considered include: GCG (alpha cells), INS (beta cells), SST (delta cells), PPY (PP cells), PRSS1 (acinar cells), KRT19 (ductal cells), COL1A1 (mesenchymal cells), and ESAM (endothelial cells). Among the clustering methods tested, CoMem-DIPHW, CoMem, and node2vec demonstrated superior performance in clustering pancreatic cell populations, since each cell-type-specific marker was distinctly expressed within the clusters defined by these methods.

We then cross-referenced the top 10 differentially expressed (DE) genes (see Table VI) identified for each CoMem-DIPHW cluster to validate these tentative labels. Cell type labels were assigned to clusters based on the expression of the gene markers in Fig. 8. Clusters where the corresponding gene markers show high expression are assigned to cell types corresponding to the gene marker. To validate our clustering results, we also match each cluster found by CoMem-DIPHW to potential cell types utilizing markers collected in the PanglaoDB cell type marker database (version 27 Mar 2020) [52]. This cell type assignment is based on the overlap between the corresponding cluster’s DE genes and the markers for each cell type, assigning a score based on the proportion of matched markers. Cell types with a score above a threshold of 0.05 were considered potential matches. Table V presents the top matches for each cluster. These results align well with our previous analysis based on marker gene distribution (Figure 8), providing additional support for our cell type assignments. The only discrepancy between the results based on PanglaoDB and the previous experiments lies in cluster 4. Matching the DE genes with PanglaoDB cell type

markers suggests Pancreatic stellate cells (PSCs) or Granulosa cells, while the COL1A1 and ESAM expression plots indicate mesenchymal or endothelial cells. However, this apparent discrepancy can be explained by the fact that PSCs can differentiate into cells with endothelial-like properties [69], and granulosa cells can exhibit mesenchymal-like behaviors [70]. Both cell types share characteristics with mesenchymal and endothelial cells, explaining the overlap in gene expression patterns observed in cluster 4.

Cluster 0 was identified as acinar cells by the high expression of PRSS1 in Fig. 8. In Table VI, the top 10 DE genes for cluster 0 include CPA1, CPA2 [71], PLA2G1B [72], CTRB1 [73], and PRSS1 [74], which are involved in the production of digestive enzymes, a primary function of pancreatic acinar cells. Clusters 2 and 7 were identified as alpha cells by the high expression of GCG. Alpha cells are responsible for glucagon secretion and blood glucose regulation [75, 76]. Markers for alpha cells among the DE genes in cluster 2 found in the PanglaoDB database include GLS, CRYBA2, FAP, LOXL4, MAFB, and RGS4. In cluster 7, alpha cell marker DE genes include LOXL4, PAX6, RGS4, and CRYBA2. Cluster 3 was classified as ductal cells by the high expression of KRT19. Six out of the 10 DE genes identified by CoMem-DIPHW are markers for ductal cells in the pancreas, including SLC4A4, ANXA4, KRT19, CFTR, CLDN1, and ONECUT2. Cluster 5 was classified as delta cells by the high expression of SST. Established markers strongly associated with delta cells in DE genes identified by CoMem-DIPHW include GAD2, PCSK1, LEPR, and CASR. Cluster 6 was classified as beta cells by the high expression of INS. This finding is also strongly supported by the its DE genes MAFA, ERO1LB, PDX1, IAPP, SYT13, HADH and ADCYAP1. Both COL1A1 and ESAM are highly expressed in cluster 4, suggesting mesenchymal or endothelial cells. These align well with 9 out of the top 10 DE genes found by CoMem-DIPHW, including COL4A2, COL4A1, SPARC, EMP1, IGFBP4, HTRA1, PXDN, LAMA4 and NID1.

Hence, the cell clusters determined by CoMem-DIPHW and identified by the canonical markers selected by the original study [46] are also strongly supported by the top DE genes of each cluster.

TABLE V. Top cell type matches for each cluster based on PanglaoDB markers

Cluster	Primary Match	Score	Secondary Match	Score
0	Acinar cells	0.188	Foveolar cells	0.095
1	Beta cells	0.078	-	-
2	Alpha cells	0.128	Glutamnergic neurons	0.100
3	Ductal cells	0.116	Ionocytes	0.091
4	Pancreatic stellate cells	0.069	Granulosa cells	0.063
5	Delta cells	0.176	Parathyroid chief cells	0.125
6	Beta cells	0.137	Delta cells	0.088
7	Alpha cells	0.085	Retinal progenitor cells	0.077
8	Gamma (PP) cells	0.103	Retinal progenitor cells	0.077

TABLE VI. Top 10 Differentially Expressed Genes for Each Cluster Identified by CoMem-DIPHW in the Human Pancreas Data [46]

Cluster 0	Cluster 1	Cluster 2	Cluster 3	Cluster 4	Cluster 5	Cluster 6	Cluster 7	Cluster 8
CPA2	ADCYAP1	GLS	LITAF	LAMA4	GAD2	ADCYAP1	KIAA1244	ABCC9
PRSS1	GEM	FAP	KRT19	NID1	RBP4	MAFA	MUC13	BCYRN1
CPA1	TGFBR3	ENPP2	ANXA4	SPARC	LEPR	NPTX2	KCTD12	PCSK1N
CPB1	SRXN1	KCTD12	LAD1	IGFBP4	HADH	HADH	PDK4	PAX6
GSTA1	NPTX2	TMEM176B	ONECUT2	EMP1	UCHL1	ERO1LB	PAX6	RGS1
PLA2G1B	HADH	RGS4	ANXA3	COL4A1	UNC5B	PDX1	TMEM176B	SPOCK1
GSTA2	UCHL1	CRYBA2	SERPING1	SERPINH1	PCSK1	IAPP	ENPP2	PRG4
PNLIP	HSPA1B	MAFB	SLC4A4	HTRA1	PRG4	SYT13	RGS4	ID2
PRSS3P2	SYT13	LOXL4	CFTR	PXDN	SORL1	PFKFB2	CRYBA2	AKAP12
CTRB1	CDKN1A	NAA20	CLDN1	COL4A2	CASR	SORL1	LOXL4	AQP3

Following discussion of the results from human pancreas dataset, we provide a brief overview of the results from the mouse pancreas, human brain, and mouse brain datasets. For these datasets, we have included visualizations in the appendix that show the average expression of the top DE genes across clusters identified by different methods, which shows our proposed algorithm's ability in effectively distinguishing cell clusters by their expression profiles. The supplements also contain tables listing the top DE genes for clusters identified by CoMem-DIPHW in each dataset for reference.

#### IV. CONCLUSION

In this study, we developed and analyzed two hypergraph-based clustering algorithms, DIPHW and CoMem-DIPHW for improved cell clustering performance on scRNA-seq data. Firstly, the Dual-Importance Preference (DIP) Hypergraph Walk (DIPHW) we developed extends the edge-dependent vertex weight (EDVW) hypergraph random walk proposed by [41], and consistently outperformed it in our experiments. DIPHW’s key idea lies in its symmetrized account of importance: it considers both the relative importance of edges to nodes and nodes to edges, or importance of genes relative to cells and cell to genes, along with a preference exponent for faster clustering.

Secondly, the CoMem and CoMem-DIPHW clustering methods we developed incorporate a Memory mechanism that considers both the abundance counts data (conceptualized as hypergraphs) and the two co-expression networks (unipartite network projections of the scRNA-seq abundance counts: gene co-expression networks and cell co-expression networks). This approach allows us to integrate both local and global information when computing embeddings for clustering.

Thirdly, we identified and showed with experiments 2 the issue of inflated signals in coexpression networks brought by sparsity of scRNA-seq data, which thus provided additional motivation for conceptualizing the scRNA-seq data as hypergraphs for embedding computation. The sparsity-induced correlation inflation leads to misleading cell connections in cell co-expression networks. Conventional correlation measures (Pearson’s, Spearman’s, Kendall’s Tau) either treat the common zeros in cell expression profiles as a sign of homogeneity or ignore them during correlation computation (as in cosine similarity). Neither strategy handles the intricacy of the data sparsity well enough to avoid suboptimal results. We showed in Tab. III D 5 that unipartite network-based clustering approaches perform poorly on correlation networks constructed using cosine similarity compared to using other correlation measures. Furthermore, unipartite network-based clustering methods generally underperform compared to hypergraph-based methods or PCA, which do not require transforming scRNA-seq count data into unipartite networks.

Fourthly, we compared our proposed methods with well-established clustering methods commonly used in scRNA-seq analysis packages. These include five embedding-based methods (PCA, Node2Vec, EDVW [41], UMAP, and tSNE) and four community detection methods (Louvain, Greedy Modularity, Infomap, and Leiden). Our clustering performance comparison experiments span comprehensive parameter regimes, with CoMem-DIPHW and DIPHW consistently delivering superior performance, especially when data modularity is weak. In these weakly modular regimes, where clusters are hardly detectable, all the established methods we used for comparison show a much more pronounced decay in performance compared to CoMem-DIPHW. For empirical analysis, we tested our algorithms on 4 real scRNA-seq datasets and 2 benchmark datasets. In these experiments, CoMem-DIPHW consistently demonstrated superior performance in differentiating and classifying distinct cell types compared to existing methods.

Fifthly, we designed a versatile simulation algorithm for scRNA-seq data that is highly customizable through its many user-specifiable parameters. This algorithm is designed to model a wide range of expression scenarios and modular structures. Notably, it incorporates intermodular coexpressions, which mimic cell-type cross-talk observed in real biological systems.

For future work, we plan to optimize the implementation of CoMem-DIPHW to reduce its memory complexity, enhancing its scalability for larger datasets. We are also interested in exploring alternative ways to incorporate the memory mechanism into the hypergraph random walk. Currently, CoMem employs a simple product approach, moving beyond the simple product used in CoMem could potentially uncover even more effective clustering strategies.



## SUPPLEMENTARY MATERIALS

## Additional Results for Mouse Pancreas Dataset



FIG. S1. Differential gene expression profiles across clustering methods in mouse pancreas scRNAseq data. The clustering performance is assessed by the differential expression (DE) of the top 10 DE genes identified for each cluster. Each row represents a clustering method, and each column corresponds to the top 10 differentially expressed (DE) genes of a specific cluster. Violin plots show the distribution of average expression levels of the top 10 DE genes across all clusters.

TABLE S1. Top 10 Differentially Expressed Genes for Each Cluster Identified by CoMem-DIPHW in the Mouse Pancreas Data [48]

Cluster 0	Cluster 1	Cluster 2	Cluster 3	Cluster 4	Cluster 5	Cluster 6
Krt8	Vim	Vgf	Igfbp7	Sparc	Cox6a2	H2-Eb1
S100a6	Sparc	Id3	Tspan8	Col4a2	Pdyn	Cd74
Anxa2	Cald1	Mafb	Mest	Plvap	Zranb2	Tmsb4x
Krt19	Col4a2	Gpx3	Arg1	B2m	Psap	B2m
H Anxa3	Anxa2	Ttr	Hhex	Ctla2a	Ubr4	Srgn
Prdx1	Col4a1	Spp1	Cd24a	Cdh5	Slc35b4	H2-Aa
Cd9	Msn	Irx1	Gpx3	Flt1	Satb1	Cyba
Clu	Ier3	Rbp4	Clu	Col4a1	Rspo4	Cytip
Krt18	Serpinh1	Serping1	Cpa2	Pecam1	Adgrl1	Ctss
Ahnak	Gm13889	Higd1a	Rbp4	Egfl7	Hmox1	Coro1a

## Additional Results for Human Brain Dataset

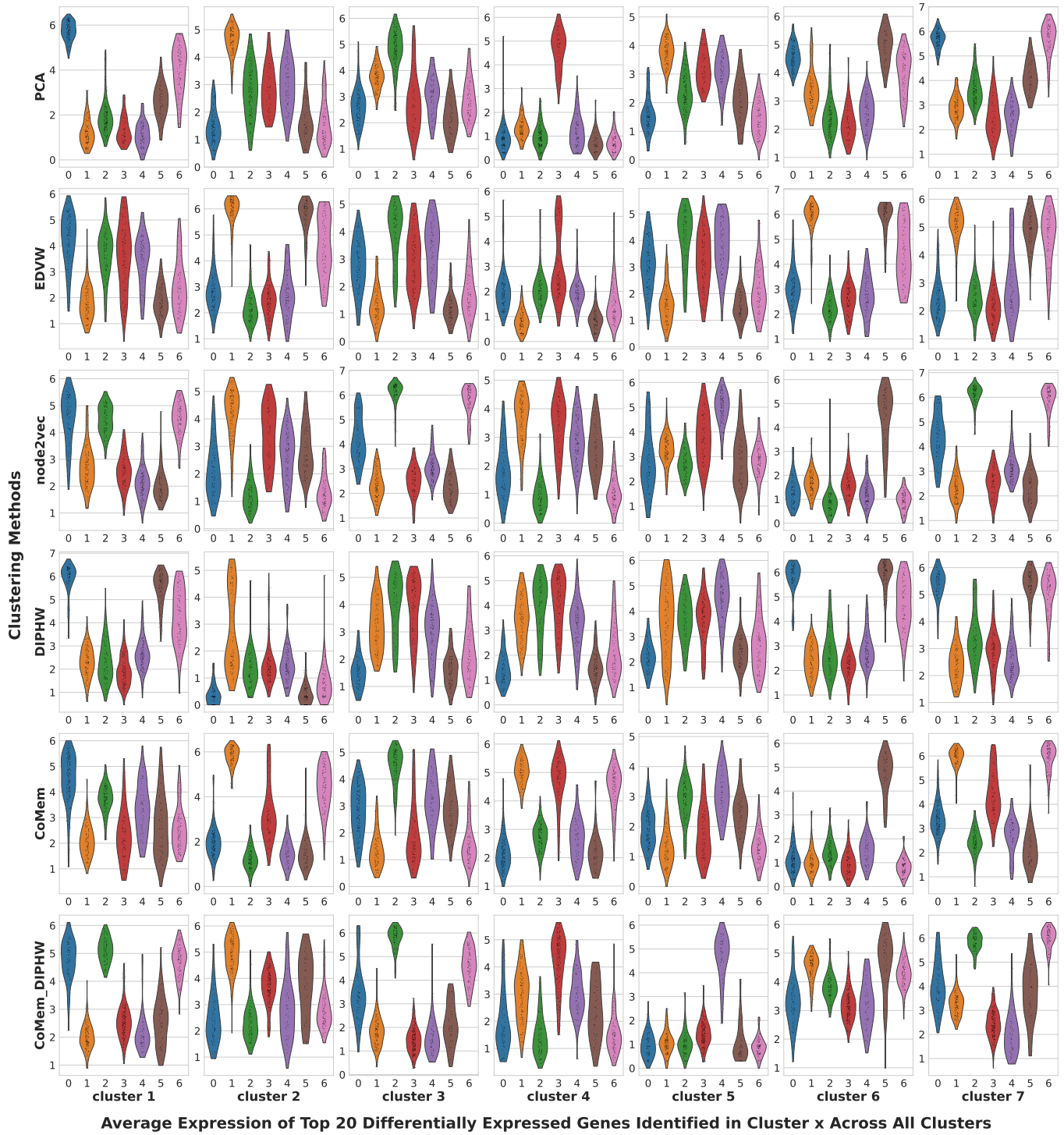


FIG. S2. Differential gene expression profiles across clustering methods in human brain scRNAseq data [45]. The clustering performance is assessed by the differential expression (DE) of the top 10 DE genes identified for each cluster. Each row represents a clustering method, and each column corresponds to the top 10 differentially expressed (DE) genes of a specific cluster. Violin plots show the distribution of average expression levels of the top 10 DE genes across all clusters.

TABLE S2. Top 10 Differentially Expressed Genes for Each Cluster Identified by CoMem-DIPHW in the Mouse Pancreas Data [45]

Cluster 0	Cluster 1	Cluster 2	Cluster 3	Cluster 4	Cluster 5	Cluster 6
PTPRM	GDAP1L1	RTN1	CDK1	COL21A1	BCL11A	CDK1
CCDC146	TAGLN3	BCL11B	C11orf31	PABPC4	NFIA	SLC1A3
RCHY1	DCC	MEF2C	SELT	COL3A1	C1orf61	PTPRZ1
LUM	GNG3	MYT1L	IMMP2L	FLRT2	SOX4	MEIS2
TXNRD1	NNAT	HMP19	TXNRD1	COL1A2	ELAVL4	CKB
SLC25A16	SOX4	LMO7	MAPK10	LUM	RASGEF1B	DCLRE1C
TRIB3	MAPK10	PDE1A	ACTL6A	MGP	NFIB	C1orf61
ZNF433	MGAT4C	GRIA2	TOP2A	DCN	STMN2	IFI44L
DCN	EBF1	ST18	MEIS1	NR4A1	BCL11B	TOP2A
TOP2A	STMN2	GAP43	HSD17B4	MFAP4	NEUROD6	DOK5

## Additional Results for Mouse Brain Dataset

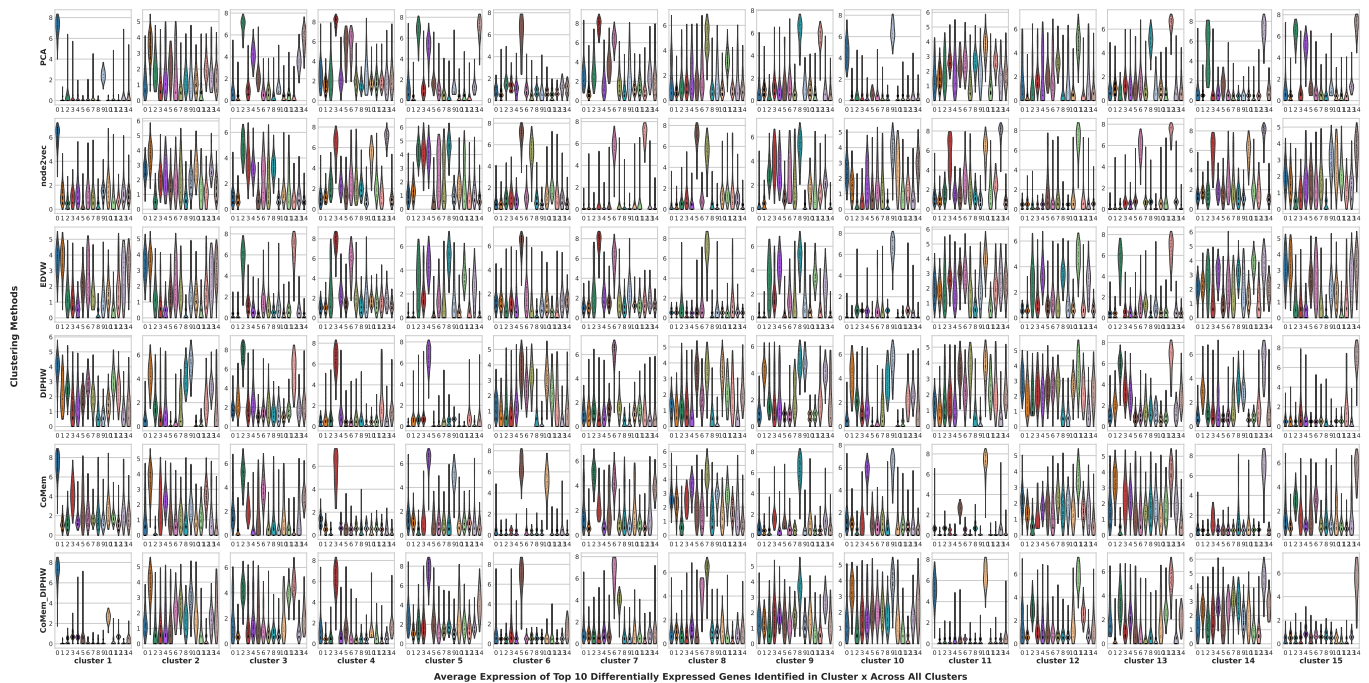


FIG. S3. Differential gene expression profiles across clustering methods in mouse brain scRNAseq data [47]. The clustering performance is assessed by the differential expression (DE) of the top 10 DE genes identified for each cluster. Each row represents a clustering method, and each column corresponds to the top 10 differentially expressed (DE) genes of a specific cluster. Violin plots show the distribution of average expression levels of the top 10 DE genes across all clusters.

TABLE S3. Top 10 Differentially Expressed Genes for Each Cluster Identified by CoMem-DIPHW in the Mouse Brain Data [47]

Cluster 0	Cluster 1	Cluster 2	Cluster 3	Cluster 4	Cluster 5	Cluster 6	Cluster 7	Cluster 8	Cluster 9	Cluster 10	Cluster 11	Cluster 12	Cluster 13	Cluster 14
Ms4a7	Efnb2	Nfasc	Pltp	Slc1a3	Tagln	Gad2	Dlx6os1	Pcp4	Kctd12	Tyrobp	Nfasc	Klk6	Pcp4	Clu
Tyrobp	Kctd12	Fa2h	Cldn5	Ntsr2	Acta2	Rab3b	Arl4c	Myo1b	Tpm1	P2ry12	Ptgds	Fa2h	Clu	Folr1
Stab1	Rgs2	Ptgds	Ly6c1	Clu	Tpm1	Crhbp	Igf1	Plxnd1	Palmd	Hexb	9630013A20Rik	Hapln2	Scg3	1700094D03Rik
Lyz2	Nr4a2	Hapln2	Ptprb	Atp1a2	Mustn1	Npy	Pnoc	Rorb	Flna	C1qa	Gpr17	S100b	Nxph3	Mia
C1qa	Cnr1	S100a6	Flt1	Gpr3711	Tpm2	Sst	Dner	Lamp5	Dner	Ctss	Gjc3	S100a6	Trp53i11	Calm4
Mrc1	Wfs1	Abhd3	Egfl7	Gja1	My19	Lgals1	Cnr1	Tnnc1	Nr4a2	C1qb	Iptr2	Gjc3	Ier5	Dynlrb2
Cbr2	Iiga8	Fosb	Sparc	Apoe	Crip1	Gad1	Slc6a1	Ier5	Wfs1	Gpr34	Mag	Sepp1	Resp18	Fam183b
Sepp1	Dcn	Gjc3	Esam	Ppap2b	Myh11	Slc6a1	Gad2	Vstm2a	Ncan	Cx3cr1	Prom1	Mag	My14	1110017D15Rik
Pf4	Nnat	Mag	Itm2a	Slc4a4	Cald1	Resp18	Vstm2a	C130074G19Rik	Rasd1	Laptn5	Rnf122	S100a1	Slc1a2	Msx1
Csf1r	Resp18	Serpnb1a	Slco1a4	Slc1a2	Mgp	Synpr	Gad1	Slc1a2	Nnat	Csf1r	Tmem141	Serpnb1a	Ablim1	Rsp1

- 
- [1] D. Szklarczyk, A. Franceschini, S. Wyder, K. Forslund, D. Heller, J. Huerta-Cepas, M. Simonovic, A. Roth, A. Santos, K. P. Tsafou, et al., *Nucleic acids research* **43**, D447 (2015).
- [2] D. V. Veres, D. M. Gyurkó, B. Thaler, K. Z. Szalay, D. Fazekas, T. Korcsmáros, and P. Csermely, *Nucleic acids research* **43**, D485 (2015).
- [3] A. Vazquez, A. Flammini, A. Maritan, and A. Vespignani, *Nature biotechnology* **21**, 697 (2003).
- [4] M. Ashtiani, A. Salehzadeh-Yazdi, Z. Razaghi-Moghadam, H. Hennig, O. Wolkenhauer, M. Mirzaie, and M. Jafari, *BMC systems biology* **12**, 1 (2018).
- [5] I. A. Kovács, K. Luck, K. Spirohn, Y. Wang, C. Pollis, S. Schlabach, W. Bian, D.-K. Kim, N. Kishore, T. Hao, et al., *Nature communications* **10**, 1240 (2019).
- [6] C. Lei and J. Ruan, *Bioinformatics* **29**, 355 (2013).
- [7] Y. Murakami, L. P. Tripathi, P. Prathipati, and K. Mizuguchi, *Current opinion in structural biology* **44**, 134 (2017).
- [8] D. J. Coleman, P. Keane, R. Luque-Martin, P. S. Chin, H. Blair, L. Ames, S. G. Kellaway, J. Griffin, E. Holmes, S. Potluri, et al., *Cell reports* **42** (2023).
- [9] G. Muzio, L. O’Bray, and K. Borgwardt, *Briefings in bioinformatics* **22**, 1515 (2021).
- [10] S. Zickenrott, V. Angarica, B. Upadhyaya, and A. Del Sol, *Cell death & disease* **7**, e2040 (2016).
- [11] M. U. Kraemer, C.-H. Yang, B. Gutierrez, C.-H. Wu, B. Klein, D. M. Pigott, O. C.-. D. W. Group†, L. Du Plessis, N. R. Faria, R. Li, et al., *Science* **368**, 493 (2020).
- [12] M. Chinazzi, J. T. Davis, M. Ajelli, C. Gioannini, M. Litvinova, S. Merler, A. Pastore y Piontti, K. Mu, L. Rossi, K. Sun, et al., *Science* **368**, 395 (2020).
- [13] J. T. Davis, M. Chinazzi, N. Perra, K. Mu, A. Pastore y Piontti, M. Ajelli, N. E. Dean, C. Gioannini, M. Litvinova, S. Merler, et al., *Nature* **600**, 127 (2021).
- [14] P. Langfelder and S. Horvath, *BMC bioinformatics* **9**, 1 (2008).
- [15] R. Satija, J. A. Farrell, D. Gennert, A. F. Schier, and A. Regev, *Nature biotechnology* **33**, 495 (2015).
- [16] A. Butler, P. Hoffman, P. Smibert, E. Papalexi, and R. Satija, *Nature biotechnology* **36**, 411 (2018).
- [17] F. A. Wolf, P. Angerer, and F. J. Theis, *Genome biology* **19**, 15 (2018).
- [18] E. Vasilyeva, A. Kozlov, K. Alfaro-Bittner, D. Musatov, A. Raigorodskii, M. Perc, and S. Boccaletti, *Scientific reports* **11**, 5666 (2021).
- [19] T. Zhou, J. Ren, M. Medo, and Y.-C. Zhang, *Physical Review E—Statistical, Nonlinear, and Soft Matter Physics* **76**, 046115 (2007).
- [20] S. S. Suzuki, Y. G. Baba, and H. Toju, *Nature Ecology & Evolution* **7**, 1432 (2023).
- [21] N. Fyhrquist, G. Muirhead, S. Prast-Nielsen, M. Jeanmougin, P. Olah, T. Skoog, G. Jules-Clement, M. Feld, M. Barrientos-Somarribas, H. Sinkko, et al., *Nature communications* **10**, 4703 (2019).
- [22] H. Eslami Manoochehri and M. Nourani, *BMC bioinformatics* **21**, 1 (2020).
- [23] E.-A. Horvát and K. A. Zweig, in *2012 IEEE/ACM International Conference on Advances in Social Networks Analysis and Mining (IEEE, 2012)*, pp. 599–606.
- [24] I. Yanai and T. Hashimshony, *Single Cell Methods: Sequencing and Proteomics* pp. 45–56 (2019).
- [25] E. Z. Macosko, A. Basu, R. Satija, J. Nemeshegyi, K. Shekhar, M. Goldman, I. Tirosh, A. R. Bialas, N. Kamitaki, E. M. Martnersteck, et al., *Cell* **161**, 1202 (2015).
- [26] G. X. Zheng, J. M. Terry, P. Belgrader, P. Ryvkin, Z. W. Bent, R. Wilson, S. B. Ziraldo, T. D. Wheeler, G. P. McDermott, J. Zhu, et al., *Nature communications* **8**, 14049 (2017).
- [27] S. Picelli, O. R. Faridani, Å. K. Björklund, G. Winberg, S. Sagasser, and R. Sandberg, *Nature protocols* **9**, 171 (2014).
- [28] B. Hwang, J. H. Lee, and D. Bang, *Experimental & molecular medicine* **50**, 1 (2018).
- [29] J. C. Marioni and D. Arendt, *Annual review of cell and developmental biology* **33**, 537 (2017).
- [30] H. Y. Wong, Q. Sheng, A. B. Hesterberg, S. Croessmann, B. L. Rios, K. Giri, J. Jackson, A. X. Miranda, E. Watkins, K. R. Schaffer, et al., *Nature Communications* **13**, 6036 (2022).
- [31] M. Laviron, M. Petit, E. Weber-Delacroix, A. J. Combes, A. R. Arkal, S. Barthélémy, T. Courau, D. A. Hume, C. Combadière, M. F. Krummel, et al., *Cell Reports* **39** (2022).
- [32] M. Karaayvaz, S. Cristea, S. M. Gillespie, A. P. Patel, R. Mylvaganam, C. C. Luo, M. C. Specht, B. E. Bernstein, F. Michor, and L. W. Ellisen, *Nature communications* **9**, 3588 (2018).
- [33] E. Landhuis, *Nature* **557**, 595 (2018).
- [34] Y. A. Lyons, S. Y. Wu, W. W. Overwijk, K. A. Baggerly, and A. K. Sood, *NPJ precision oncology* **1**, 26 (2017).
- [35] J. Ermann, D. A. Rao, N. C. Teslovich, M. B. Brenner, and S. Raychaudhuri, *Nature Reviews Rheumatology* **11**, 541 (2015).
- [36] W. Chung, H. H. Eum, H.-O. Lee, K.-M. Lee, H.-B. Lee, K.-T. Kim, H. S. Ryu, S. Kim, J. E. Lee, Y. H. Park, et al., *Nature communications* **8**, 15081 (2017).
- [37] R. Jiang, T. Sun, D. Song, and J. J. Li, *Genome biology* **23**, 31 (2022).
- [38] M. Huang, J. Wang, E. Torre, H. Dueck, S. Shaffer, R. Bonasio, J. I. Murray, A. Raj, M. Li, and N. R. Zhang, *Nature methods* **15**, 539 (2018).
- [39] P. Qiu, *Embracing the dropouts in single-cell rna-seq analysis. nat. commun. 11*, 1169 (2020).
- [40] T. H. Kim, X. Zhou, and M. Chen, *Genome biology* **21**, 196 (2020).
- [41] U. Chitra and B. J. Raphael, in *Proceedings of the 36th International Conference on Machine Learning, ICML 2019, 9-15 June 2019, Long Beach, California, USA*, edited by K. Chaudhuri and R. Salakhutdinov (PMLR, Long Beach, California, USA, 2019), vol. 97 of *Proceedings of Machine Learning Research*, pp. 1172–1181.
- [42] M. J. Barber, *Physical Review E—Statistical, Nonlinear, and Soft Matter Physics* **76**, 066102 (2007).
- [43] K. Pearson, *The London, Edinburgh, and Dublin Philosophical Magazine and Journal of Science* **2**, 559 (1901).

- [44] A. Grover and J. Leskovec, in *Proceedings of the 22nd ACM SIGKDD international conference on Knowledge discovery and data mining* (2016), pp. 855–864.
- [45] J. G. Camp, F. Badsha, M. Florio, S. Kanton, T. Gerber, M. Wilsch-Bräuninger, E. Lewitus, A. Sykes, W. Hevers, M. Lancaster, et al., *Proceedings of the National Academy of Sciences* **112**, 15672 (2015).
- [46] M. J. Muraro, G. Dharmadhikari, D. Grün, N. Groen, T. Dielen, E. Jansen, L. Van Gurp, M. A. Engelse, F. Carlotti, E. J. De Koning, et al., *Cell systems* **3**, 385 (2016).
- [47] A. Zeisel, A. B. Muñoz-Manchado, S. Codeluppi, P. Lönnerberg, G. La Manno, A. Juréus, S. Marques, H. Munguba, L. He, C. Betsholtz, et al., *Science* **347**, 1138 (2015).
- [48] M. Baron, A. Veres, S. L. Wolock, A. L. Faust, R. Gaujoux, A. Vetere, J. H. Ryu, B. K. Wagner, S. S. Shen-Orr, A. M. Klein, et al., *Cell systems* **3**, 346 (2016).
- [49] L. Tian, X. Dong, S. Freytag, K.-A. Lê Cao, S. Su, A. JalalAbadi, D. Amann-Zalcenstein, T. S. Weber, A. Seidi, J. S. Jabbari, et al., *Nature methods* **16**, 479 (2019).
- [50] A. Ianevski, A. K. Giri, and T. Aittokallio, *Nature communications* **13**, 1246 (2022).
- [51] X. Zhang, Y. Lan, J. Xu, F. Quan, E. Zhao, C. Deng, T. Luo, L. Xu, G. Liao, M. Yan, et al., *Nucleic acids research* **47**, D721 (2019).
- [52] O. Franzén, L.-M. Gan, and J. L. Björkegren, *Database* **2019**, baz046 (2019).
- [53] V. Y. Kiselev, T. S. Andrews, and M. Hemberg, *Nature Reviews Genetics* **20**, 273 (2019).
- [54] M. D. Luecken and F. J. Theis, *Molecular systems biology* **15**, e8746 (2019).
- [55] E. Armingol, A. Officer, O. Harismendy, and N. E. Lewis, *Nature Reviews Genetics* **22**, 71 (2021).
- [56] C. Zhang, Y. Hu, and L. Gao, *Scientific Reports* **13**, 15746 (2023).
- [57] J. A. Zepp and E. E. Morrisey, *Nature reviews Molecular cell biology* **20**, 551 (2019).
- [58] D. Bayik and J. D. Lathia, *Nature Reviews Cancer* **21**, 526 (2021).
- [59] A. Lehuen, J. Diana, P. Zacccone, and A. Cooke, *Nature Reviews Immunology* **10**, 501 (2010).
- [60] T. S. Andrews, V. Y. Kiselev, D. McCarthy, and M. Hemberg, *Nature protocols* **16**, 1 (2021).
- [61] M. Xu, *SIAM Review* **63**, 825 (2021).
- [62] A. Duò, M. D. Robinson, and C. Soneson, *F1000Research* **7** (2018).
- [63] G. Huguet, A. Tong, E. De Brouwer, Y. Zhang, G. Wolf, I. Adelstein, and S. Krishnaswamy, *Advances in Neural Information Processing Systems* **36** (2024).
- [64] V. Y. Kiselev, K. Kirschner, M. T. Schaub, T. Andrews, A. Yiu, T. Chandra, K. N. Natarajan, W. Reik, M. Barahona, A. R. Green, et al., *Nature methods* **14**, 483 (2017).
- [65] D. Kobak and P. Berens, *The art of using t-sne for single-cell transcriptomics. nat commun* **10**, 5416 (2019).
- [66] C. N. Heiser and K. S. Lau, *Cell reports* **31** (2020).
- [67] L. McInnes, J. Healy, and J. Melville, *arXiv preprint arXiv:1802.03426* (2018).
- [68] I.-H. Ham, D. Lee, and H. Hur, *Cancers* **13**, 1172 (2021).
- [69] L. Cheng, M. Xie, W. Qiao, Y. Song, Y. Zhang, Y. Geng, W. Xu, L. Wang, Z. Wang, K. Huang, et al., *Communications Biology* **4**, 1039 (2021).
- [70] M. Jozkowiak, G. Hutchings, M. Jankowski, K. Kulcenty, P. Mozdziak, B. Kempisty, R. Z. Spaczynski, and H. Piotrowska-Kempisty, *Cells* **9**, 1418 (2020).
- [71] K. Tamura, J. Yu, T. Hata, M. Suenaga, K. Shindo, T. Abe, A. MacGregor-Das, M. Borges, C. L. Wolfgang, M. J. Weiss, et al., *Proceedings of the National Academy of Sciences* **115**, 4767 (2018).
- [72] D. Y. Hui, *Biochimica et Biophysica Acta (BBA)-Molecular and Cell Biology of Lipids* **1864**, 784 (2019).
- [73] A. V. Pinho, I. Rooman, M. Reichert, N. De Medts, L. Bouwens, A. K. Rustgi, and F. X. Real, *Gut* **60**, 958 (2011).
- [74] E. Masson, J.-M. Chen, M.-P. Audrézet, D. N. Cooper, and C. Férec, *PloS one* **8**, e73522 (2013).
- [75] I. Quesada, E. Tudurí, C. Ripoll, and A. Nadal, *Journal of endocrinology* **199**, 5 (2008).
- [76] E. Gylfe and P. Gilon, *Diabetes research and clinical practice* **103**, 1 (2014).